Water and energy fluxes within the EUMETSAT Climate Monitoring SAF: Evapotranspiration and Latent and Sensible Heat Fluxes

MOUTIER WILLIAM[1], CLERBAUX NICOLAS[1], ARBOLEDA ALIRIO[1], BARRIOS JOSE-MIGUEL[1], GELLENS-MEULENBERGHS FRANÇOISE[1], MOREELS JOHAN[1], BOURGEOIS QUENTIN[2], TETZLAFF ANKE[2], SCHRÖDER MARC[3], AND TRIGO ISABEL[4]

[1] *RMI Royal Meteorological Institute of Belgium, Brussels, Belgium*
[2] *Federal Office of Meteorology and Climatology MeteoSwiss, Zürich, Switzerland*
[3] *Deutscher Wetterdienst, Offenbach, Germany*
[4] *Instituto Portugus do Mar e da Atmosfera (IPMA), Lisbon, Portugal*
[*] *william.moutier@meteo.be*

Compiled May 22, 2023

http://dx.doi.org/10.1364/ao.XX.XXXXXX

ABSTRACT

Climate data records are fundamental to understand and explain long term trends and processes. This study presents the latent (LE) and sensible (H) heat flux climate data record committed by the Satellite Application Facility on Climate Monitoring. Retrievals are obtained thanks to an adapted version of the methodology developed by the Land Surface Analysis Satellite Application Facility. The method has been adapted from the Tiled ECMWF Scheme for Surface Exchanges over Land model allowing use of satellite-based data and numerical weather prediction models' outputs as forcing. CM SAF product is provided over the Meteosat disk (65°N/S and 65°W/E) at hourly, daily, monthly time-step with a spatial resolution of 0.05 degrees (regular grid). CM SAF data cover 38 years: from 1983 to 2020. LE and H have been validated against reference data records from observation sources (30 stations from FLUXNET2015 and ICOS datasets), reanalysis (ERA5 and GLDAS) and satellite-based product (LSA SAF and GLEAM). Overall, when comparing with eddy covariance data, bias were of -9.7 (-10.8, -12.32) W m^{-2} for hourly (daily, monthly) latent heat flux and 1 (-2.6, -2.8) W m^{-2} for sensible heat flux. The unbiased root mean square difference was found to be 32.5 (24.7, 19.7) W m^{-2} for hourly (daily, monthly) latent heat flux, and 48.5 (34.1, 23.6) W m^{-2} for sensible heat flux. Largest uncertainties of latent heat flux and sensible heat fluxes were during day time and for southern regions (latitude lower than 16°N).

1. INTRODUCTION

In the context of global warming and rapid changes of the land use by human economical activities, it is fundamental to be able to accurately estimate and understand trends of key variables as sensible (H) and latent (LE) heat fluxes. LE and H are result from the partitioning of available net radiation energy at the ground surface, and this feedback is influenced by a variety of factors, including soil temperature, moisture content, and other physical and biological characteristics of the vegetation type. The sensible heat flux represents the amount of energy transferred by convection and/or conduction from the surface to the atmosphere [1, 2]. The amount of energy and water consumed by evaporation corresponds to the latent heat flux and the evapotranspiration processs [1, 3]. By materializing the exchange of water and energy from the earth surface to the atmosphere, the latent and sensible heat fluxes control the development of the planetary boundary layer and govern land-atmosphere interaction [4, 5]. They play a major role in the hydrological cycle [6], carbon cycle [7] and surface energy balance [8]. Thus, various applications such as water resource management, agricultural planning, weather forecasting, drought/flood detection, etc, are possible thanks to their estimations ([9, 10] and reference there in). For instance, monitoring of H and LE allows the detection of desertification, monsoon circulation and climate change e.g. [11–13]. Therefore, getting homogeneous long-term time series (at least few decades) and catching both long and natural or human induced short-scale trends of turbulent heat fluxes is crucial.

In situ measurements, reanalyse and/or satellite-based datasets are data sources of surface heat fluxes. While *In situ* flux tower measurements dataset e.g. FLUXNET network (Pastorello et al., 2020) are fundamental, global trend analysis require reanalysis and/or satellite-based products. Reanalyse products (e.g. ERA5, ERA-Land or GLDAS) are gridded, global, and provide long/stable time series with a high temporal resolution (Hourly or 3-Hourly). However, estimations issued from atmospheric-land model coupled as ERA5 remains modelled-based and the quality/quantity of observations assimilated into the system change over time [14]. Long-term satellite-based data records appear to be a good compromise with estimations at high spatial (< 10 km) and/or high temporal resolutions (< 3 h)

at the large scale (e.g. Meteosat grid or global). Worth noting that accuracy of satellite-based fluxes depends on the quality of input data itself and are limited by the accuracy of retrieval algorithms. Thus, estimations may differ according to the selected input/model. Large number of studies evaluated heat fluxes models (e.g. MOD16, SEBAL, SEBS, GLEAM, etc.) with RMSE between 10 and 140 W m^{-2} (roughly between 5% and 50% of the mean observed value) [4, 15–34]. From an assessment of 30 published validations, Kalma et al., (2008) observed an average RMSE of about 50 W m^{-2} and relative typical error of 15-30%. Su et al., (2007) assessed the Surface Energy Balance System (SEBS) model and ET predictions based on MODIS Land Surface Temperature plus Coordinated Enhanced Observing Period (CEOP) meteorological observations or Global Land Data Assimilation System (GLDAS) forcing. For MODIS based ET estimation, RMSEs between 61 and 141 W m^{-2} (up to 50% of the mean observed values) were obtained. Concerning sensible heat fluxes estimated from the SEBS model, RMSEs ranged from 26 to 57 W m^{-2} (20 to 60% of the mean observed values) were calculated. Study from Loew et al., (2016) evaluated the High resOlution Land Atmosphere surface Parameter from Space (HOLAPS) latent heat flux estimates with 48 FLUXNET worldwide stations. Overall the RMSE was 51.2 (30.7) W m^{-2} for hourly (daily) latent heat flux, and 84 (38) W m^{-2} for sensible heat flux when compared against measurement stations.

Specific initiative like the WAter Cycle Multi-mission Observation Strategy-EvapoTranspiration (WACMOS-ET) project has been created to derive and intercompare ET estimates from satellites, using different methodologies, in order to develop a predictive capability for terrestrial ET, [4, 35]. Results showed an inter-product variability even when common forcing is used. This latter pointed out the difficulty for a single model to perform better considering all type of conditions. In addition, via an online questioner, the WACMOS-ET -project, showed that for roughly 30% of the users, real-time or near real-time availability is crucial. Indeed, the users' communities and GCOS-requirements (e.g. [34] and GCOS-244) tends to request sub-daily data records of LE/H while most the satellite-based products provide daily-integrated datasets computed from polar satellite data. Sub-daily resolution is desirable in evaporation modelling to investigate the land–atmosphere interactions during the daily cycle of the planetary boundary layer [4]. Products providing sub-daily data exist but do not necessarily cover several decades. For example, HOLAPS [30] and the product developed by the Land Surface Analysis SAF (LSA SAF) [36] provide near-real time (NRT) latent and sensible heat fluxes but cover only 2 decades with the periods 1998-2015 and 2005-2022, respectively.

In this frame, the Satellite Application Facility on Climate Monitoring (CM SAF) of EUMETSAT develops satellite-derived products to support the understanding of the climate. During the Third Continuous Development and Operations Phase (CDOP3), the CM SAF is extending its product portfolio with a Climate Data Record (CDR) based on two sensors of the Meteosat suite of geostationary satellites: the Meteosat Visible and InfraRed Imager (MVIRI) and the Spinning Enhanced Visible and InfraRed Imager (SEVIRI). The Regional Land Fluxes CDR provides, over a period of almost 40 years (1983-2020), various parameters depicting the surface states and radiation fluxes, including the Surface Radiation Balance (SRB), the Cloud Fractional Cover (CFC), the Land Surface Temperature (LST), the Evapotranspiration (ET) and the Latent (LE) and Sensible (H) Heat Fluxes. The CDR has been built in collaborations between CM SAF, LSA SAF and the EUMETSAT Secretariat ensuring the uniqueness of this product and the consistency among its parameters. The data are provided hourly, daily and monthly (plus the monthly mean diurnal cycle) over a regular grid covering the Meteosat Disk (65°N–65°S and 65°W–65°E)at a spatial resolution of 0.05 degrees (i.e. about 5.5 km) from 1983 to 2020. The current study introduces the new latent and sensible heat flux CDR of the CM SAF, including the validation. The surface heat fluxes have been validated against reference data from observation sources (30 stations from FLUXNET2015 and ICOS datasets), reanalysis (ERA5 and GLDAS) and satellite-based product (LSA SAF and GLEAM). The paper is organized as follows: Sect. 2 short description of the algorithm and its inputs; in Sect. 3 the results of the validations and specific analyse of the stability according to the regions is performed, followed by the summary and conclusions.

2. MATERIALS AND METHODS

This section describes the main inputs data and the most conceptual approach of the retrievals. Main step and equations are presented in Sect A. please note that a detailed Algorithm Theoretical Basis Document [37] fully describes the methodology and the processing chain.

A. Algorithm overview

To create the current dataset, surface latent and sensible heat fluxes (and the evapotranspiration) are retrieved by using an adapted version of the methodology developed by the Land Surface Analysis Satellite Application Facility (LSA SAF) CDR recently released [36, 44]. This latter can be described as a Surface Vegetation-Atmosphere Transfer (SVAT) scheme modified to accept input data from external sources [45, 46]. The algorithm has been adapted from the Tiled ECMWF (European Centre for Medium-Range Weather Forecasts) Scheme for Surface Exchanges over Land (TESSEL) model [47, 48] and H-TESSEL [49] allowing the use of satellite-based data and numerical weather prediction (NWP) models' outputs (ECMWF reanalysis) as forcing. All details about CM SAF (pre)processing of the data inputs can be seen in [37]. In a nutshell, the algorithm is an energy balance model aiming to partition the available energy between LE, H and heat conduction flux into the ground (G). Each elementary spatial unit of the algorithm is called pixel in reference to the basic unit of the Meteosat Visible and InfraRed Imager (MVIRI) and the Spinning Enhanced Visible and Infrared Imager (SEVIRI), onboard of, respectively, Meteosat First and Second Generation (MFG and MSG) satellites. Considering the fact that evapotranspiration process and heat exchanges depend on the land cover (surface type), each pixel is split up into a maximum of 4 tiles. The fraction of each tile is calculated from the LC map see Sect. A. Twelve different land cover types are considered in the algorithm (listed in the Table 5 in Sect. A). Thus, for each tile, a closure of the surface energy budget is obtained. The surface energy balance is computed by the algorithm at tile level in a conceptual layer, called skin layer. This latter represents the coverage of the land as a flat layer, witfhout description of the 3-D structure of the canopy. The final fluxes are calculated separately for each tile and the final pixel value is obtained by a weighted contribution of all tiles composing it. Note that Given the non-linear inter-dependency between the unknowns, an iterative procedure is used to solve the system. Iteration is stopped when pixel estimates of latent and sensible heat fluxes are numerically stabilized.

Table 1. Main inputs variables used in the CM SAF algorithm.

Variable name (shortname; unit)	Source	Spatial resolution	Temporal resolution	Period / Area covered	Reference
Surface Incoming Shortwave radiation (*SIS*; W m^{-2})	CM-23271	0.05°	15 (MSG) - 30min (MFG)	1983- 2020 /Meteosat disk	[38]
Surface Downward Longwave radiation (*SDL*; W m^{-2})	CM-23271	0.05°	15 (MSG) - 30min (MFG)	1983- 2020 /Meteosat disk	[38]
Surface Albedo (*SAL*)	CM-23271	0.05°	15 (MSG)- 30min (MFG)	1983- 2020 /Meteosat disk	[38]
Leaf Area Index (*LAI*; m^2 m^{-2})	GLOBMAP	0.08°	8 – 16 days	1981-2019 / Global	[39, 40]
Land Cover (*LC*)	ESA-CCI	300m	Yearly	1992-2020 / Global	[41, 42]
Tree height (h_{tree}, m)	NASA/JPL	1 km	Static	Static / Global	[43]
Meteorological data (Ta, Td, U, V, Pa, etc.) & Surface soil moisture	ERA5	0.25°	Hourly	1979-2019 / Global	[14]

B. Inputs data

All inputs used in the algorithm are listed in Table 1. A full description of each of them is given in the following subsections.

B.1. MeteoSat data

Observations from MVIRI and the SEVIRI are used as inputs for all radiation components including the Surface Incoming Solar radiation (SIS), the Surface Albedo (SAL) and the Surface Downward Longwave radiation (SDL) - which are jointly retrieved using the CM SAF software "GeoSatClim". Full description of the calculations are presented in [38]. Please note that the albedo is set to 0.1 for inland water and limited to 0.5 for snow.

B.2. Tree height

Tree height (h_{tree}, m) is a static map over the MFG and MSG period, derived from the global 1km forest canopy height developed at NASA/JPL. This global canopy height map was created using 2005 data from the Geoscience Laser AltimeterSystem (GLAS) aboard ICESat (Ice, Cloud, and land Elevation Satellite) [43]. Basically, based on 1 km data, average canopy height has been calculated for each MFG/MSG pixel.

B.3. ESA CCI Land Cover dataset

The European Spatial Agency (ESA) Climate Change Initiative Land Cover (CCI-LC) climate data record [41, 42] has been used to calculate the land cover fractions of the 4 main tiles composing the MFG/MSG pixels. The land cover map product is provided globally from 1992 to 2022 at 300m/yearly spatial-temporal resolutions in a Plate Carrée projection. The original dataset is composed of 36 classes allowing a discrimination of the land cover at regional scale. The CCI-LC project developed a user toolbox allowing adjustment in the product. With this toolbox (v3.14), area of interest is extracted (latitude: [-65, 65]; longitude: [-65, 65]) and a reclassification from the Land Cover Classification System (LCCS) classes to the 12 surface types considered in the algorithm, based on a Look-Up-Table (adapted from Table 7.2 in [41]), have been performed. Second, the surface type of the 4 main tiles of each MFG/MSG pixel are determined as well as their fraction area (ξ_i). Note that vegetation types are not 100% covered by vegetation as bare soil contributes to each of them (Table 1 in [47]). Thus, fraction areas are recalculated by considering the bare soil contribution then, the four main tiles are reordered if needed.

B.4. Meteorological data

Hourly 2 m air temperature (Ta), 2 metre dew-point temperature (Td), 10 m wind speed (U, V), mean sea level pressure (MSL), soil type (SLT), soil temperature level (1 to 4; stll), volumetric soil water content layer (1 to 4) and geopotential data extracted from ERA5 Re-Analysis database [14] at 0.25°. ERA5 is the fifth generation of global atmospheric reanalysis generated by the ECMWF. ERA5 is produced from the ECMWF's Integrated Forecast System (IFS) cycle 41r2 using the four-dimensional variational data assimilation (4D-Var) and the Land Data Assimilation System (LDAS) to assimilate, respectively, atmospheric and land data. First, a bilinear reprojection from native grid to the MFG/MSG grid and a linear interpolation every 30/15 min is performed to get the values at 0.05°. Then, specific calculations are made to get: the total wind speed, the topographic correction for temperature, the relative humidity and the soil moisture (see details in Sect A).

B.5. LAI GLOBMAP dataset

To get the Leaf Area Index (LAI) value of each MFG/MSG pixel, the long term Global Mapping (GLOBMAP) LAI Version 3 dataset has been chosen. This latter, generated by the Chinese Academy of Sciences, provides half-month (during 1980-2000) or 8 days (during 2001-2020) LAI values over a 40 years' period (1980-2020) with a spatial resolution of 0.08° (~ 8km) [39, 40, 50]. A bilinear reprojection is performed to the MFG/MSG pixel. From 8-15 days values, a 'weighted mean' daily value is calculated for each pixel by applying a Gaussian filter to remove potential noise. The Gaussian distribution (G) in 1-D has the form:

$$G(\Delta t) = \frac{1}{\sigma\sqrt{2\pi}} \exp\left(\frac{(\Delta t)^2}{2\sigma^2}\right) \quad (1)$$

where, Δt is the time difference in days between the desired date and the day of the LAI values in the dataset at specific time and σ (equal to 5) is the standard deviation of the distribution. Only images of the dataset being in a time windows of ±30 days are used to calculate the final "weighted mean". The following equation is used to make the calculation:

$$\mathrm{LAI_{pix}} = \sum_{n=0}^{m} \frac{G(\Delta t_n)}{\sum_{n=0}^{m} G(\Delta t_n)} \times \mathrm{LAI}_n \quad (2)$$

with, m the number total of images being in the 30 days time window and LAI_n the corresponding value at specific time. In addition, to take into account the surface type, a specific processing is performed to calculate the LAI value of each i^{th} tile (LAI_i). Calculation is performed for all vegetation tiles and a value of 0 is adopted for other surface types. The LAI_i is calculated for each tile composing the pixel by applying this equation:

$$\mathrm{LAI}_i = \alpha \times \mathrm{LAI}_{LUT,i} \quad (3)$$

with,

$$\alpha = \frac{\mathrm{LAI_{pix}}}{\sum \xi_i \times \mathrm{LAI}_{LUT,i}} \quad (4)$$

where, ξ_i, LAI_i, LAI_{Pix} and $\mathrm{LAI}_{LUT,i}$ are, respectively, the area fraction of the i^{th} tile, the LAI of the tile, the LAI of the pixel and the LAI of the tile obtained from a predefined LUT which depend on the surface type of the tile. To build this LUT, four steps have been followed: i) Calculate the monthly mean values; ii) Extract all pixels, from the LAI GLOBMAP dataset, considered as "homogeneous", i.e. where the fraction area of the dominant surface type is higher than 60% (it was not possible to raise the limit higher than 60% as we don't have enough pixel in this case for grassland type); iii) Separate all different vegetation surface types; iv) For each surface type, calculate the mean values over four specific areas: South Africa (latitude: [-40.48°, 0.2°], longitude: [7.66°, 79.03°]), North Africa (latitude: [0.19°, 39.39°], longitude:[-21.66°, 79.83°]), Europe (latitude: [34.49°, 81.26°], longitude: [-46.05°, 78.33°]) and South America (latitude: [-37.56°, 12.62°], longitude: [-81.2°, -32.82°]). Thus we get monthly $\mathrm{LAI}_{\mathrm{LUT,i}}$ values representative of each surface type for various regions of the world.

C. Validation datasets

The products used for model's evaluation have been selected according to their temporal coverage and their spatial and temporal resolutions. The Table 2 summarizes the characteristics of all datasets used to validate the CDR (see details about each product in the following sub-sections).

C.1. In situ datasets (FLUXNET2015/ICOS)

In situ measurements used as reference dataset were extracted from the FLUXNET2015 dataset (https://fluxnet.fluxdata.org) and from the Integrated Carbon Observation System (ICOS) international platform (https://www.icos-cp.eu). While the FLUXNET2015 and ICOS networks provide data from 212 stations (117 in the field of view of METEOSAT) we selected 30 of them to perform analysis. Four criteria were used to select the stations: i) well established stations and already used datasets by the LSA SAF; ii) data quality and representativeness [55]; iii) ability to sample different climates and biomes; and iv) spatial homogeneity of the station. Localizations of selected sites in this report are shown in Figure 2. An overview of the sites can be found in Table 7 (i.e. climate, area, available years etc.).

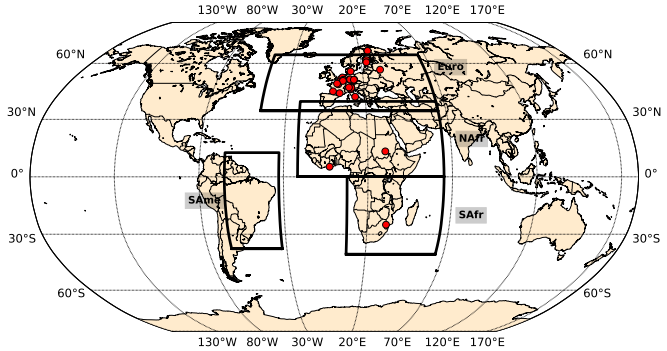

Fig. 1. Location of eddy covariance stations used to evaluate the CM SAF dataset. Black frames delineate: Europe (Euro; lat:[34.49,60], lon:[-46.05, 60]), North-Africa (NAfr; lat:[0.19, 39.39], lon:[-21.68, 60]), South-Africa (SAfr; lat:[-40.48, 0.2], lon:[7.68, 60]) and South-America (SAme; lat:[-37.56,12.62], lon:[-60, -32.82]) areas (LSA SAF regions).

At each site, turbulent fluxes data are gap-filled using the marginal distribution sampling (MDS) method [56] and are available at half-hourly (local time), daily and monthly time scales (full description in [51] and https://fluxnet.org/data/fluxnet2015-dataset/dataprocessing). Eddy covariance measurements do not allow an energy balance closure (EBC; the sum of latent and sensible fluxes equal to net radiation minus ground heat flux). The energy imbalance can be between 10 and 30% (average 20%) (e.g. [23, 57–60]). The CM SAF dataset getting a closure, we use corrected variables, named "LE_CORR" and "H_CORR", which are calculated thanks to a closure correcting factor differing according to the time resolution and assuming a correct Bowen ratio [23, 51, 61]. For each time-step, different quality control, are provided to ensure the quality level of the gap-filling. For half-hourly data, quality control values of 0 (measured), 1 (good), 2 (medium) or 3 (bad). For daily and monthly data, fractions between 0-1 indicate the percentage of measured and good quality gap-filled data. To minimize potential differences due to poor quality measurements we extracted data with a quality control of 1 ("good quality") for half-hourly data, and 100% of good data for daily and monthly data.

The station's half-hourly data are hourly averaged and an offset is applied to get the hour in UTC and not in local time. Note that use exclusively data with a quality control of 1 was not possible to calculate the monthly mean diurnal cycle because not enough match-up is obtained. Thus, values with associated quality control of 1 and 2 (good and medium) have been used in this case.
It is worth-noting that *in situ* measurements are subject to typical error between 10% and 30% [16, 23, 57, 62–67].

C.2. ERA5 dataset

As mentioned previously, ERA5 [14] is the fifth generation of global atmospheric reanalysis generated by the ECMWF. The land surface model used is the land Hydrology Tiled ECMWF Scheme for Surface Exchanges over Land (HTESSEL). This later demonstrated its performance to simulate surface turbulent heat fluxes in offline experiments [49, 68, 69]. All global atmospheric, oceanic and land surface fields are available at an hourly time step with a spatial resolution of 0.25° (~32km) covering the period from January 1950 to present, thus the full extend of the record.

Table 2. Main characteristics of datasets use for the validation.

	FLUXNET2015 - ICOS	ERA5	GLDAS v2.0	GLEAM v3.5a	LSA SAF
Variable(s) available	LE-H	LE-H	LE-H-ET	ET	LE-H-ET
Spatial resolution	point	0.25°	0.25°	0.25°	0.05°
Temporal resolution used for comparisons	hourly daily monthly	hourly	daily monthly	daily monthly	daily monthly
Period covered used for comparisons	-	1983-2020	2000-2020	1983-2020	2004-2020
Product type	Eddy-covariance	Reanalyse	Reanalyse	Satellite-based	Satellite-based
References	[51]	[14]	[52]	[53, 54]	[36, 44]

Specific analysis of the land-surface energy partitioning in ERA5 has been performed in [70]. Comparison at station showed that ERA5 tends to overestimate LE with Mean difference around 10 W m^{-2}. ERA5 appeared to be almost unbiased for sensible heat flux (minor underestimation).

C.3. GLDAS dataset

Global Land Data Assimilation System version 2 (GLDAS; [52]) is a new generation of reanalysis developed jointly by the National Aeronautics and Space Administration (NASA) Goddard Space Flight Center (GSFC) and National Center for Environmental Prediction (NCEP). GLDAS, which has been streamlined and parallelized by the Land Information System (LIS; [71]), generates land surface products by using various offline (not coupled to the atmosphere) land surface models (LSM) and ingesting satellite- and ground-based observational datasets [52]. Details about the forcing data and description of the model are available on http://disc.Sci.GSFC.NASA.Gov/Hydrology. Currently, GLDAS has three components: GLDAS-2.0 (1948-2014), GLDAS-2.1 (2000- Present), and GLDAS-2.2 (Fev 2003-Present). Beyond their differences in term of forcing or data assimilation source, the choice of the product has been dictated by the period covered to validate the CM SAF product. GLDAS 2.0, 2.1 and 2.2 cover, respectively, 31, 20 and 17 years. Thus, we selected the "open-loop" (i.e. no data assimilation) GLDAS-2.0 product with a daily and monthly (averaged from 3 hourly) temporal resolution. GLDAS-2.0 has been forced entirely with the Princeton meteorological forcing input [72] and the data has been simulated by the Noah Model 3.3 [73, 74] in Land Information System Version 7 with a spatial resolution of 0.25°.

C.4. LSA SAF dataset

As mentioned in the Sect A, the LSA SAF and the CM SAF core model is similar and only the forcing differ. For instance, while ERA5 is used as input to get the soil moisture in the CM SAF code, while the H SAF dataset is used in the LSA SAF approach. Other difference can be seen in the retrieval of the LAI for each tile. Indeed, an inversion matrix approach is used in the LSA SAF [36, 44] while an LUT approach is adopted here (see Sect. B.5). All details about CM SAF (pre)processing of the data inputs can be seen in the RD 1 documents. Finally, the minimal stomatal resistance (Rsmin) value for evergreen broadleaved trees tile is of 140 in the LSA SAF model and of 200 in the CM SAF model.

C.5. GLEAM dataset

The Global Land Evaporation Amsterdam Model (GLEAM; [53, 54]) is a remote sensing-based model allowing the estimation of the terrestrial evapotranspiration components (transpiration, bare soil evaporation, interception loss, and sublimation) and root-zone soil moisture. To correct random forcing errors, and other potential effects such as irrigation, that are not explicitly modeled in GLEAM, observations of surface soil moisture are also assimilated into the soil profile. Interception loss is calculated separately in GLEAM using a Gash's analytical model ([75] and reference therein). Finally, the potential evapotranspiration is calculated using the Priestley-Taylor (PT) equation [76], and then, the actual evapotranspiration is obtained by including stress factors such as soil moisture states and vegetation physiological characteristics. The key distinguishing features of this model are the use of microwave-derived soil moisture, land surface temperature and vegetation density, and the detailed estimation of rainfall interception loss. Here, we use GLEAM V3.5 data globally at daily and monthly temporal resolutions with a spatial resolution of 0.25°.

Note that to analyse the stability of the latent in flux in Sect. C, the GLEAM dataset, monthly ET values (mm month^{-1}) from GLEAM have been converted in W m^{-2} by assuming a temperature of 20°C :

$$LE(W\ m^{-2}) = \frac{ET(mm\ month^{-1}) \times L_v(20^o)}{3600 * 24 * N_{Day}} \quad (5)$$

where N_{Day} is the number of day in the month and L_v the latent heat of vaporisation (Eq. 47).

C.6. Statistical metrics

The CDR is evaluated in terms of bias and unbiased root mean square difference (uRMSD). The the mean absolute relative difference (MARD) and the mean absolute difference (MAD), were also used as statistic metrics:

$$\text{Bias} = \frac{1}{N} E_i - M_i \quad (6)$$

$$\text{RMSD} = \left[\frac{(E_i - M_i)^2}{N} \right]^{1/2} \quad (7)$$

$$\text{uRMSD} = \left[(\text{RMSD})^2 - (\text{Bias})^2 \right]^{1/2} \quad (8)$$

$$\text{MARD}\ (\%) = \frac{100}{N} \times \frac{|E_i - M_i|}{M_i} \quad (9)$$

Table 3. Performance statistics of hourly, daily and monthly CM SAF latent heat flux dataset as compared to FLUXNET2015/ICOS observations at 30 stations for different seosons and day/night conditions.

	N	<FLUXNET2015 | ICOS> ($W\,m^{-2}$)	<CMSAF> ($W\,m^{-2}$)	Bias ($W\,m^{-2}$)	uRMSD ($W\,m^{-2}$)
		Hourly			
DJF[a]	174598	8.6	-2.2	-6.5	22.9
MAM[a]	122072	29.7	18	-11.7	36.5
JJA[a]	120042	49.7	36.9	-12.8	44.2
SON[a]	149168	17.5	8.2	-9.3	26.6
Day	214847	55.3	37.1	-18.2	49.6
Night	323476	5.1	0.7	-4.4	10.9
Overall	565880	24.2	14.5	-9.7	32.5
		Daily			
DJF	24357	8	3	-5	14.44
MAM	26138	42.7	32.1	-10.6	25.16
JJA	27293	77.4	61.5	-15.9	33.9
SON	27335	26.2	15.3	-10.9	19
Overall	105123	39.4	28.6	-10.8	24.7
		Monthly			
DJF	747	9	3	-5.9	12.1
MAM	825	44.8	32.2	-12.6	18.8
JJA	853	79.3	62.3	-17.1	26.4
SON	870	28.1	15.1	-12.9	16.4
Overall	3295	41.2	28.8	-12.32	19.7

[a] DJF: December January February; MAM: March April May; JJA: June July August; SON: September October November.

$$\mathrm{MAD} = \frac{1}{N} \times |E_i - M_i| \quad \textbf{(10)}$$

Where N is the number of estimations/measurements and E and M represent the estimated and measured (or reference) values, respectively. For uRMSD and bias calculations, reference values correspond to the FLUXNET2015/ICOS data for comparison at station while they are all other dataset values (LSA SAF, ERA5, GLDAS and GLEAM) for inter-product comparisons.

3. RESULTS AND DISCUSSION

A. Validation at stations

A.1. Latent heat flux

Figures 2-4; display the bias (top panels) and the uRMSD (bottom panels) of selected products (CM SAF, ERA5, LSA SAF and GLDAS) as compared to *in situ* FLUXNET2015/ICOS data for hourly, daily and monthly latent heat flux datasets, respectively. Performance metrics presented have been calculated from a subset including only observations with common matchups for all products. Thus, performance metrics can be directly compared between products.

Results show that CM SAF biases are, on average over all stations, of -11 W m^{-2}, -13 W m^{-2} and -14 W m^{-2} for hourly, daily and monthly time step, respectively. Both LSA SAF and CM SAF data tend to underestimate *in situ* observations. Considering all time-step, CM SAF data have higher biases than other datasets. The mean biases at all stations (N=90) is of -13 W m^{-2} for CM SAF while it is of -3 W m^{-2} (N=90) 4 W m^{-2} (N=90) and 3 W m^{-2} (N=60) for LSA SAF, ERA5 and GLDAS, respectively. Concerning uRMSD, average of 31 W m^{-2}, 23 W m^{-2} and 17 W m^{-2} are calculated for hourly, daily and monthly data, respectively. Note that considering all temporal resolution, the Skukuza station appears to be the localization where the worst uRMSD results are obtained. Some doubts about corrections applied to close the energy budget during the FLUXNET processing (see Sect C.1) would need to be raised as bias is and uRMSD are linearly correlated with the correction applied (R^2 of 0.98, N=950; Figure not showed here). Worth noting that uRMSD values obtained for the CM SAF dataset are in-line with other dataset performances. Indeed, results obtained from CM SAF and all other products differ, on average, of 1.3% (N=240). In addition, results consistent with the literature [30, 54, 77–81]. For instance, by comparing estimations from 7 land surface models to eddy correlation measurements in China, Guo et al., 2022 calculated bias values from -14.27 to -2.93 W m^{-2} and uRMSD ranged from 29.8 W m^{-2} to 39.3 W m^{-2}.

These various observations are confirmed with the detailed statistics table (Table 3) which includes performance statistics for all available matchups between CM SAF and *in situ* data (no restriction with other datasets) for different time resolutions and periods. Globally, similar results are observed for bias and uRMSDs. As expected, better absolute results are obtained in the winter season (DJF period in the table as most of the stations are in Europe) and during the night. The bias and the uRMSD are on average 2.7 and 2.2 times higher in summer than in winter. In addition, bias and uRMSD are, respectively, 4.1 and 4.6 times better during the night than the day. Those observations tend to indicate better absolute retrievals for low value cases. Please note that if we look at relative errors, the model performs better for high value cases. For instance, the bias -6.5 W m^{-2} observed in winter represents a relative error of 76% as compared to mean *in situ* value while, the bias of -12.8 W m^{-2} in summer represents only 26% of the mean *in situ* value. It is worth noting that an underestimation is obtained for all considered cases (seasons, day/night and overall). Deeper investigation would be required in the future to find the source of this negative bias and adapt the model or the inputs accordingly.

A.2. Sensible heat flux

Figures 5-7 display the bias (top panels) and the uRMSD (bottom panels) of selected products (CM SAF, ERA5, LSA SAF and GLDAS) as compared to *in situ* FLUXNET2015/ICOS data for hourly, daily and monthly sensible heat flux datasets. Performance metrics presented have been calculated from a subset including only observations with common matchups for all products.

Concerning the bias, over all the stations, average values of -2 W m^{-2}, -0.7 W m^{-2} -0.2 W m^{-2} is obtained for hourly, daily and monthly data, respectively. CM SAF sensible heat flux is almost unbiased with mean bias, over all time-step and stations, of -1 W m^{-2} (N=90). Other product slightly underestimate the sensible heat flux with mean biases of -5 W m^{-2} (N=90), -7 W m^{-2} (N=90) and -10 W m^{-2} (N=60) for LSA SAF, ERA5 and GLDAS datasets, respectively. Concerning the precision (uRMSD), the average values over all stations are of 47 W m^{-2}, 28 W m^{-2} and 18 W m^{-2} for hourly, daily and monthly data, respectively. Please note

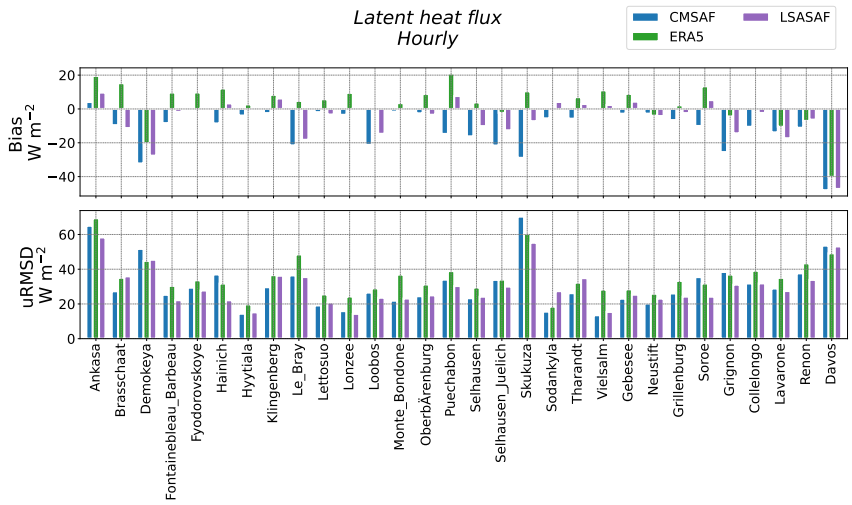

Fig. 2. Bar plot showing the hourly bias (W m^{-2}; top) and the hourly unbiased root mean square error (W m^{-2}; bottom) of CM SAF (blue), ERA5 (green) and LSA SAF (violet) datasets as compared to FLUXNET2015/ICOS dataset at stations for the latent heat flux.

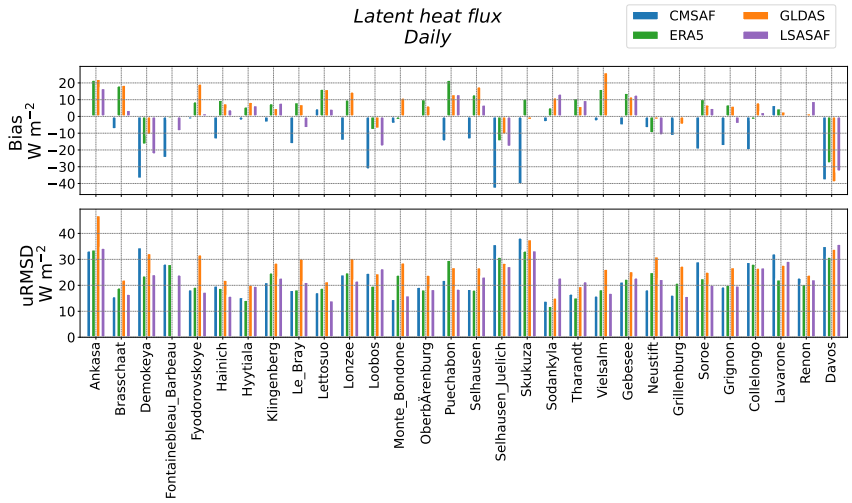

Fig. 3. Bar plot showing the daily bias (W m^{-2}; top) and the daily unbiased root mean square error (W m^{-2}; bottom) of CM SAF (blue), ERA5 (green), GLDAS (orange) and LSA SAF (violet) datasets as compared to FLUXNET2015/ICOS dataset at stations for the latent heat flux.

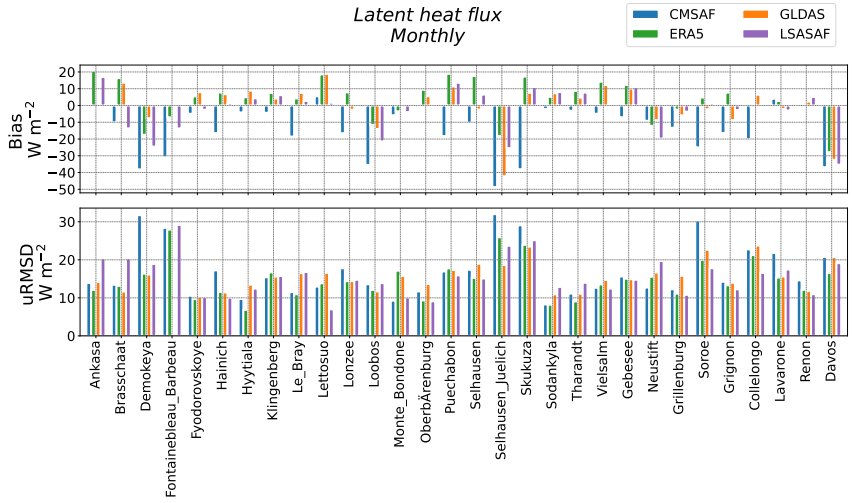

Fig. 4. Same as Fig. 3 but for monthly latent heat flux.

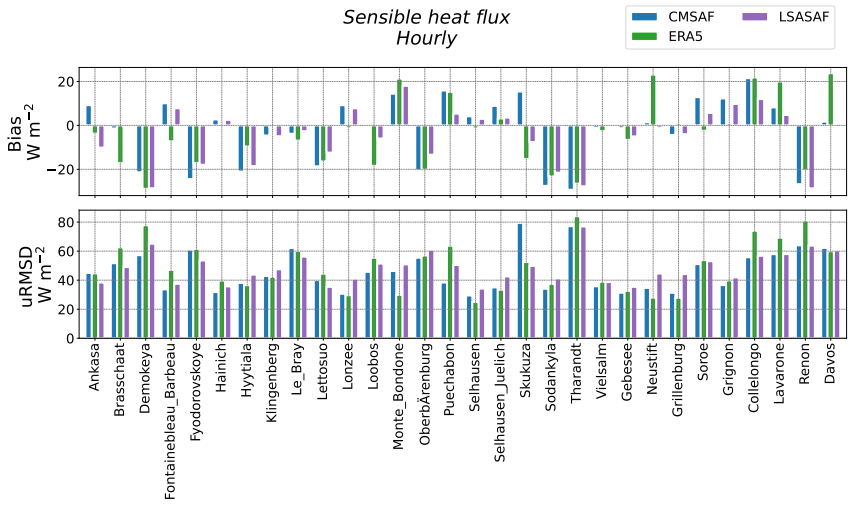

Fig. 5. Bar plot showing the hourly bias (W m^{-2}; top) and the hourly unbiased root mean square error (W m^{-2}; bottom) of CM SAF (blue), ERA5 (green) and LSA SAF (violet) datasets as compared to FLUXNET2015/ICOS dataset at stations for the sensible heat flux.

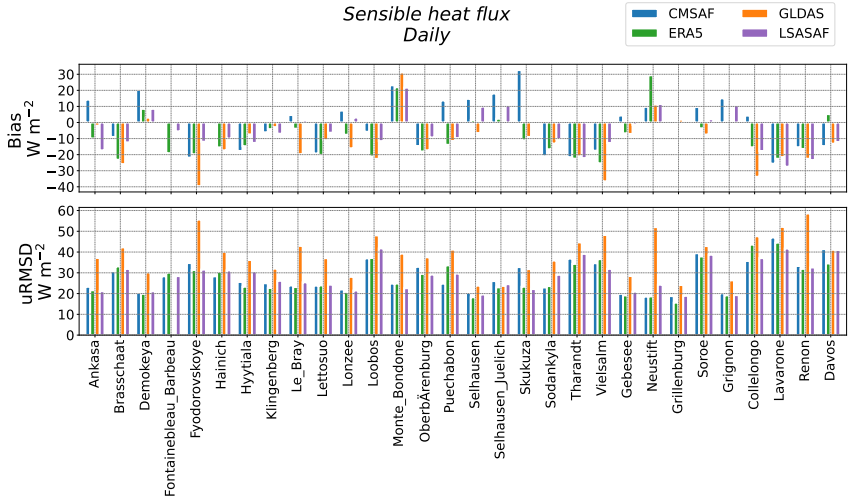

Fig. 6. Bar plot showing the daily bias (W m^{-2}; top) and the daily unbiased root mean square error (W m^{-2}; bottom) of CM SAF (blue), ERA5 (green), GLDAS (orange) and LSA SAF (violet) datasets as compared to FLUXNET2015/ICOS dataset at stations for the sensible heat flux.

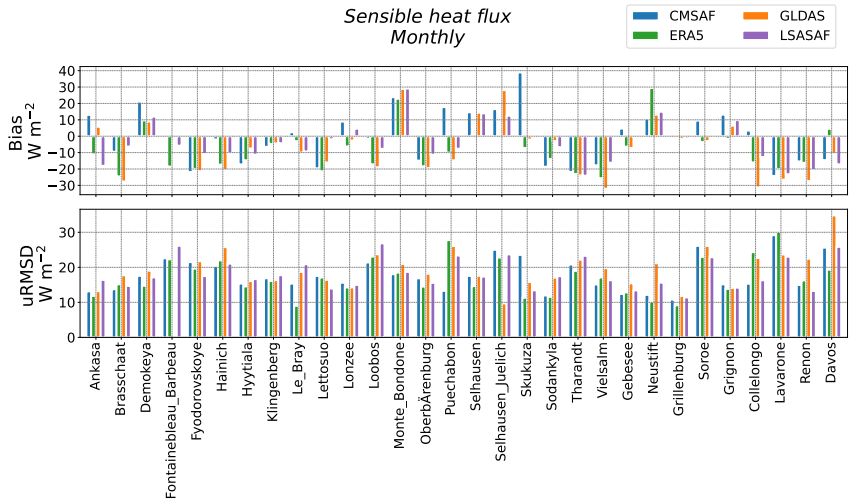

Fig. 7. Same as Fig. 6 but for monthly latent heat flux.

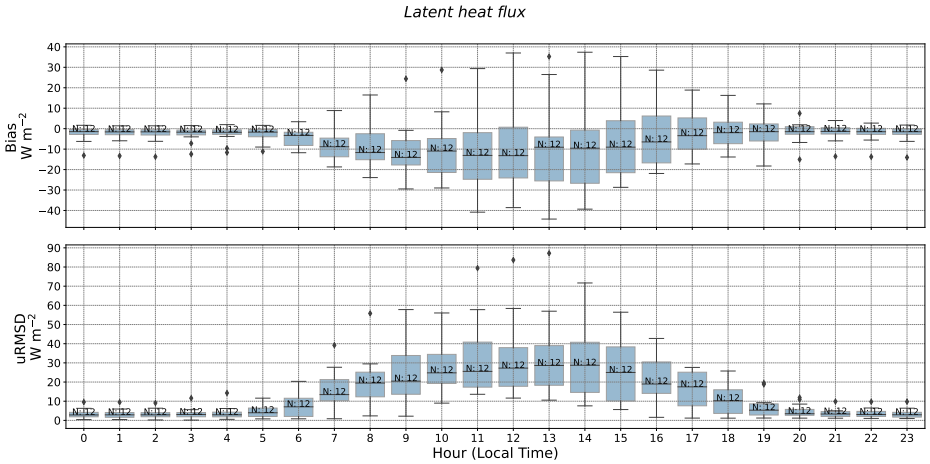

Fig. 8. Box plots displaying the monthly mean diurnal cycle bias (W m^{-2}; top panel) and uRMSD (W m^{-2}; top panel) for the latent heat flux at FLUXNET2015/ICOS stations. The height of the box indicates the Interquartile range (IQR) of values, the horizontal line inside the box indicates the median value, the upper box level indicates the upper quartile (75^{th} percentile; Q3), the lower box level indicates the lower quartile (25^{th} percentile; Q1), bars (whiskers) indicate the minimum and maximum values, dots indicate the outliers (higher than Q3 + 1.5*IQR or lower than Q1 – 1.5*IQR).

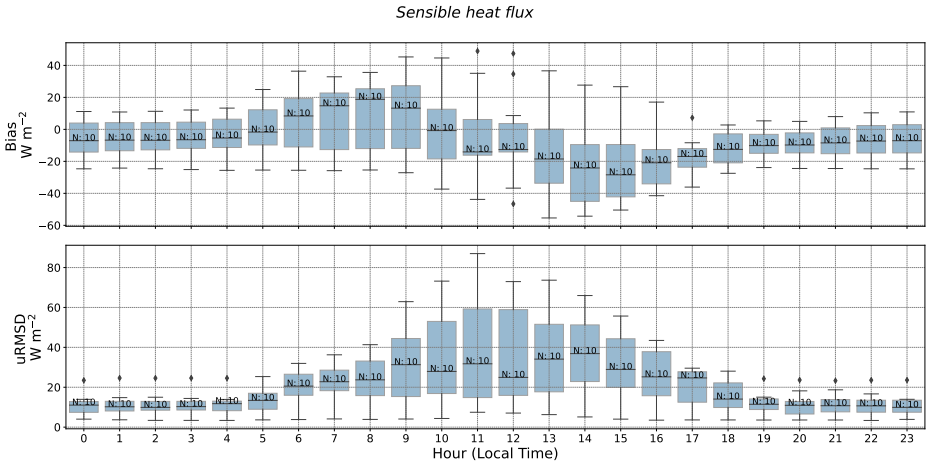

Fig. 9. Same as Fig. 8 but for sensible heat flux.

Table 4. Performance statistics of hourly, daily and monthly CM SAF sensible heat flux dataset as compared to FLUXNET2015/ICOS observations at 30 stations for different seasons and day/night conditions.

	N	<FLUXNET2015 | ICOS> ($W\,m^{-2}$)	<CM SAF> ($W\,m^{-2}$)	Bias ($W\,m^{-2}$)	uRMSD ($W\,m^{-2}$)
		Hourly			
DJF[a]	133541	-9.1	-10.7	-1.7	37.7
MAM[a]	88058	17	18.5	+1.5	57.7
JJA[a]	85010	26.4	25.8	-0.6	60.9
SON[a]	106625	-3	2	+4.9	39.9
Day	168175	46.1	53.4	+7.2	69.2
Night	226285	-22.5	-26	-3.5	25
Overall	413234	5.4	6.3	+1	48.5
		Daily			
DJF	25817	-2.6	-5.3	-2.7	24.1
MAM	27222	41.2	35.7	-5.5	39
JJA	28385	48.1	42	-6.1	42.9
SON	28443	8.8	12.4	+3.6	24.5
Overall	109867	24.3	21.7	-2.6	34.1
		Monthly			
DJF	817	-3.9	-5.7	-1.8	19.4
MAM	864	42.8	35.6	-7.2	25.6
JJA	910	48.5	41.6	-6.9	28.3
SON	921	6.8	11.5	+4.6	16.9
Overall	3512	24	21.2	-2.8	23.6

[a] DJF: December January February; MAM: March April May; JJA: June July August; SON: September October November.

that CM SAF uRMSD values at stations are in the same order of magnitude than other products. Results obtained from CM SAF and all other products differ, on average, of -3% (N=240). In addition, results for our comparison with FLUXNET2015/ICOS is in the same order of magnitude as reported in previous studies [30, 77, 79, 81, 82]. For instance, Loew et al., 2016 obtained, while comparing sensible heat flux (from HOLAPS) with data at 48 FLUXNET stations, RMSDs between 38 and 84 W m^{-2} for hourly and daily data.

The Table 4 presents the performance metrics between CM SAF and FLUXNET2015/ICOS data including all possible matchups for all stations for different time resolutions and periods. Daily and monthly data tend to underestimate the sensible heat flux (bias between -1.8 W m^{-2} and -6.9 W m^{-2}) except in autumn (~ +4 W m^{-2}). No clear significant bias is observed for the hourly product. Please note that the low mean values for hourly data (6 W m^{-2}) as compared to daily and monthly data (23 W m^{-2}) is due to the high number of night cases. Concerning the precision (uRMSD), as observed for the LE, the model has a better absolute accuracy for low values cases (night and winter) than high values cases (day and summer). For instance, the uRMSD values in of 69 W m^{-2} during the day while it is of 25 W m^{-2} during the night.

A.3. Evaluation of the monthly mean diurnal cycle at station

The monthly mean diurnal cycle values have been evaluated by comparing CM SAF with FLUXNET2015/ICOS values. As noticed in the Sect. C.1, the quality control at FLUXNET2015/ICOS stations has been relaxed to medium (QC value of 1 or 2) due to the miss of match-up.

Figures 8 and 9 display the box plots of the distributions of bias, and uRMSDs calculated at all considered stations of the monthly mean diurnal cycle for the latent and the sensible heat flux. Note that for the validation, the hours are local time. Concerning the latent heat flux (Fig. 8), Bias and uRMSD follow, respectively, an inverted bell curve and a bell curve. As observed previously, the latent heat flux is underestimated with mean bias values between -1.7 W m^{-2} at 6 p.m. and -10.9 W m^{-2} at 9 a.m. Highest discrepancies are obtained from 7 a.m. and 5 p.m. (mainly day time) with most of the bias values around -7.8 W m^{-2}, and uRMSD around 25.8 W m^{-2}, respectively. During the night, bias and uRMSDs are, respectively, around -2.5 W m^{-2} (N=13, SD=0.7 W m^{-2}) and 4.9 W m^{-2} (N=13, SD=2.4 W m^{-2}).

For the sensible heat flux (Fig. 9), similar trends are observed for the uRMSD with third quartiles forming a bell-shaped curve around noon. Mean values are between 10.7 W m^{-2} (N=10) at 11 p.m. and 39 W m^{-2} (N=10) at 11 a.m.. From 8 a.m. to 5 p.m., values are around 31.2 W m^{-2} (N=10) and they are around 13.1 W m^{-2} (N=14) for the rest of the day for the uRMSD. Concerning the bias, values follow a sinusoidal curve (sin(Hour/4)) with an overestimation during the morning and underestimation in the afternoon. Interquartile range of values (full boxes) are between -23 W m^{-2} (N=10) at 3 p.m. and 10 W m^{-2} (N=10) at 9 a.m..

B. Product inter-comparison at 0.25°

Based on level 3 daily means, we carried out comparisons between the CM SAF datasets (LE, H and ET) and other reference datasets (ERA5, LSA SAF, GLDAS and GLEAM). As a reminder, daily mean CM SAF data have been derived from 24 hourly data. Daily data are directly available for all datasets used for comparison, no integration has been made. However, CM SAF and LSA SAF have been spatially aggregated from 0.05° to 0.25° to match with ERA5, GLDAS and GLEAM datasets.

For each variable, two approaches have been used to assess the accuracy and the precision of the CM SAF products over the full disk.

1. Time series of the daily bias and uRMSD averaged over the full disk.

2. Images of the daily bias and uRMSD averaged over the year 2005.

For time series analysis, in order to avoid variation in the performance metric due to missing data, the minimum number of valid pixels has been determined as the first percentile of the corresponding record.

The following performance analysis and comparisons with requirements should be considered carefully. Comparisons performed thereafter involve biased assumptions that inter-compared products have perfect accuracy and precision.

B.1. Latent heat flux

Grid-based comparisons, carried out over the full disk for the year 2005 (MSG; Fig. 10), show an underestimation over most of the globe (top panel in Fig. 10). Bias is lower for latitudes higher than 16°N (e.g., average values of -11.8 W m^{-2} for ERA5 comparison) than southern latitudes (e.g., average value of -28.2

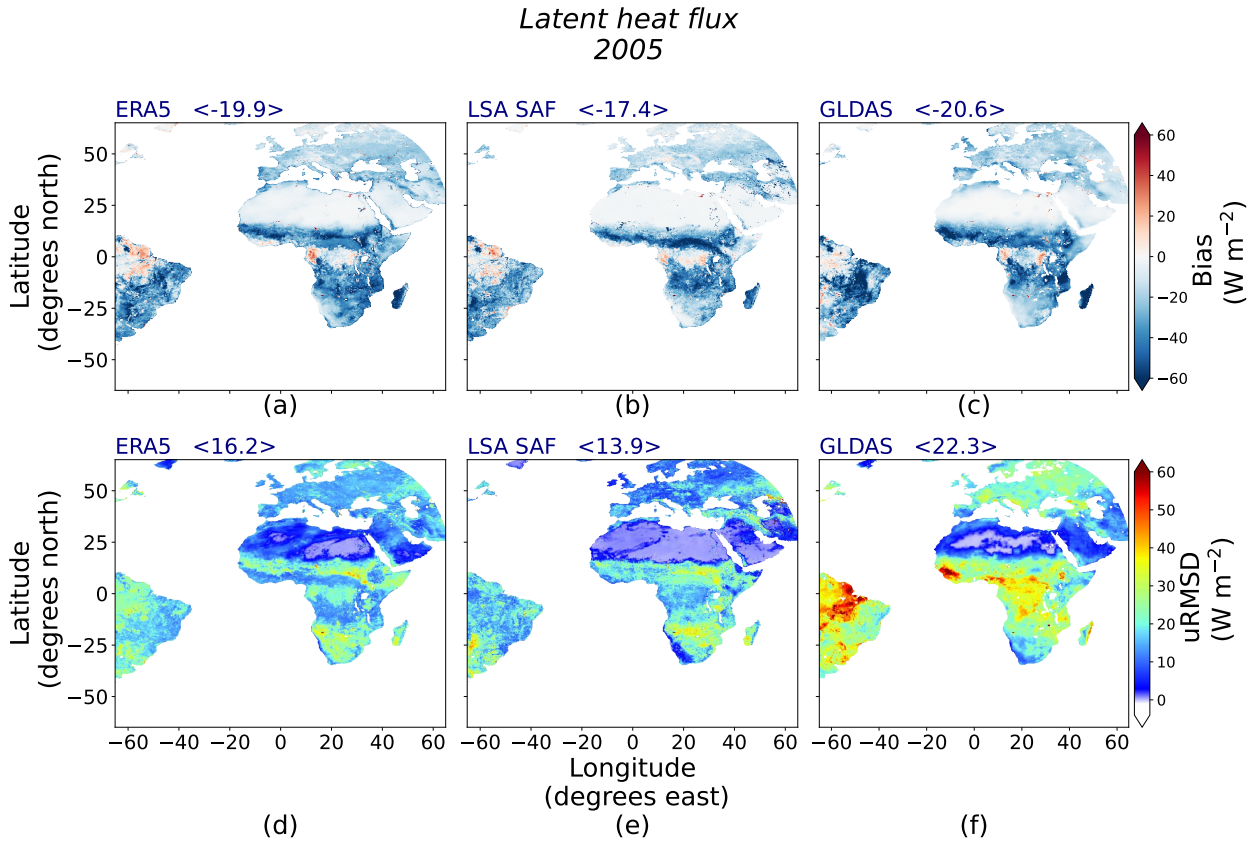

Fig. 10. Maps of averaged daily bias (top) and unbiased root mean square difference (bottom) of the surface latent heat flux (W m^{-2}) over the year 2005 of CM SAF dataset as compared to ERA5 (a-d) LSA SAF (b-e) and GLDAS (c-f) datasets at 0.25°. Average value over the map is indicated in blue over each map.

W m^{-2} for ERA5 comparison). Specific areas around the equator in South America and Africa have bias around 0. They both correspond to evergreen broadleaved trees (EBT) land cover cases (Figure not showed here). Around the EBT region in Africa, larger underestimations are observed for all products. For LSA SAF comparison, patches of high values correspond to pixels where the decidious broadleaved trees land cover are used in the processing. The differences are most probably due to differences in land cover type used as input in LSA SAF dataset. For instance, according to the land cover, the minimal stomatal resistance would directly impact LE via the canopy resistance factor (see Sect. B).

Concerning uRMSD, lowest values (dark blue areas in the graph) are found for desert areas (latitudes between 16N° and 35N°) for all the products. For the rest of the map, uRMSD values calculated when comparing CM SAF with GLDAS retrievals differ from comparison results obtained with other datasets. Indeed, uRMSD, averaged over the map, obtained for GLDAS is about 50% higher than the uRMSD calculated for LSA SAF and ERA5 map. In addition, patches of values higher than 40 W m^{-2} are only present for GLDAS comparison in South America and in the north-west of Africa regions.

B.2. Evapotranspiration

Grid-based analysis for the year 2005 (MSG; Fig. 11) shows a global underestimation between -0.52 mm day^{-1} (GLEAM) and -0.73 mm day^{-1} (GLDAS). Map of GLEAM bias (Figure 11a) is more homogeneous as compared to bias obtained with LSA SAF and GLDAS datasets. Indeed, the interquartile is of 0.65 mm day^{-1} for the GLEAM dataset while, interquartiles of 0.92 mm day^{-1} and 0.85 mm day^{-1} are observed for LSA SAF and GLDAS datasets, respectively. At the opposite, as observed for LE, larger negative bias patches are present for southern regions (latitude lower than 16°N) except for two evergreen broadleaved trees land cover regions in South America and West Africa. In addition, same patch of low values is observed for decidious broadleaved trees land cover.

Concerning uRMSD, lowest values (dark blues color) are found for desert areas (latitudes between 16°N and 35°N) for all the products. For the rest of the map, uRMSD values calculated when comparing CM SAF with GLDAS retrievals differ from comparison results obtained with other datasets. Indeed, the map averaged uRMSD of GLDAS is ∼50% higher than LSA SAF and ERA5 values. In addition, patches with values around 1.5 mm day^{-1} in South America and in the north-west of Africa regions are only present in GLDAS comparison.

B.3. Sensible heat flux

Grid-based comparisons, carried out for the year 2005 over the full disk (MSG; Fig. 12), show average bias of 3.1 W m^{-2}, 6.1 W m^{-2} and 3.0 W m^{-2} for ERA5, LSA SAF and GLDAS datasets, respectively. Similarly to LE analysis, distinction can be made between values obtained for latitude higher and lower than 16°. For instance, for ERA5 comparison, an average bias value of -1 W m^{-2} is calculated for latitudes higher than 16°N while it is of 13 W m^{-2} for lower latitudes. In those southern regions, two

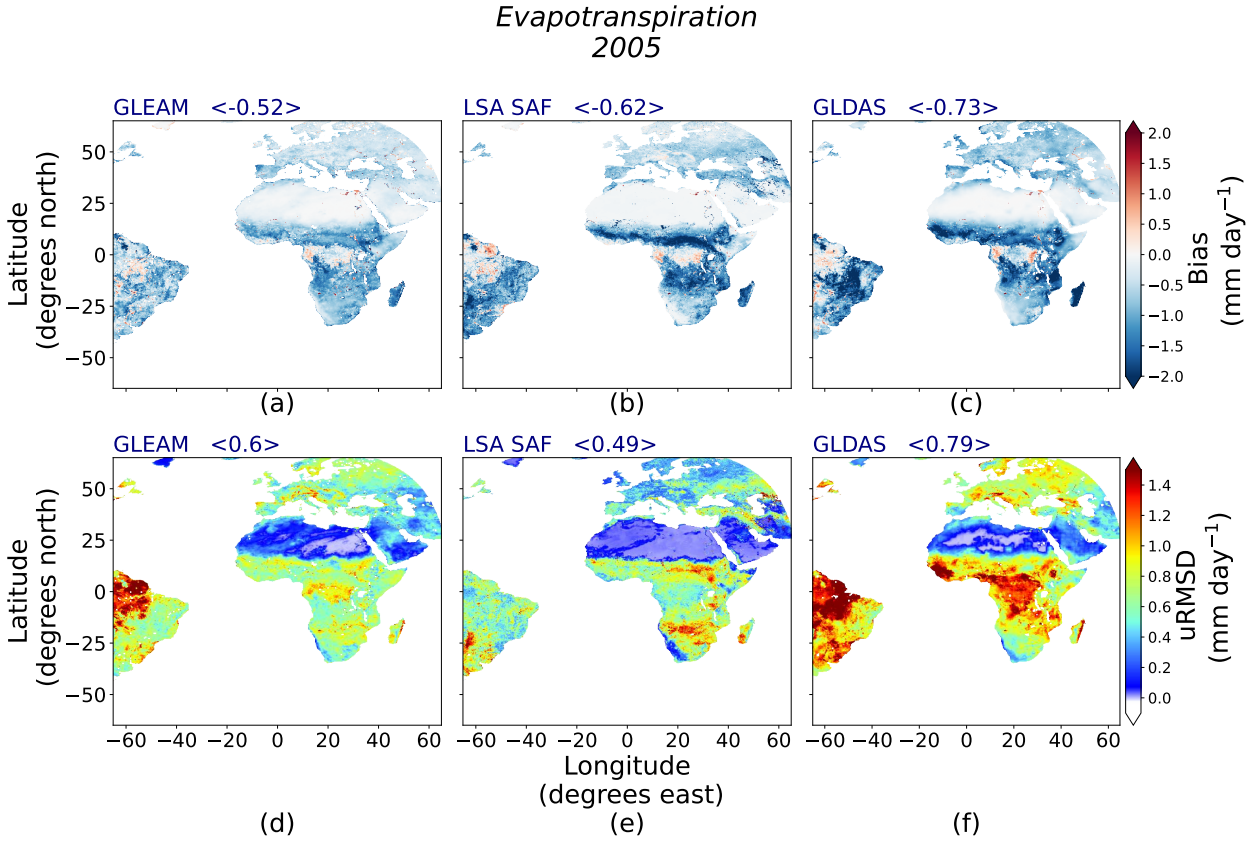

Fig. 11. Maps of averaged daily bias (top) and unbiased root mean square difference (bottom) of the evapotranspiration (mm day^{-1}) over the year 2005 of CM SAF dataset as compared to GLEAM (a-d), LSA SAF (b-e) and GLDAS (c-f) datasets at 0.25°. Average value over the map is indicated in blue over each map.

specific areas around the equator in South America and Africa tend to have negative bias. They both correspond to evergreen broadleaved trees land cover cases. Concerning uRMSD, as observed for LE, lowest values around 10 W m^{-2} (dark blues color) are found for desert areas (latitudes between 16°N and 35°N). Localizations of higher value patches are similar for all products. However, absolute uRMSD values calculated when comparing CM SAF with GLDAS retrievals differ from comparison results obtained with other datasets. Indeed, the average uRMSD if 17.8 W m^{-2} and 13.3 W m^{-2} for ERA5 and LSA SAF datasets and 24.3 W m^{-2} for GLDAS.

C. Stability

C.1. Latent heat flux

Figure 13 shows the monthly mean deseasonalized bias, averaged over the full disk, between CM SAF and ERA5, LSA SAF, GLDAS and GLEAM latent heat flux values. Over the whole period, the mean deseasonalized bias values are of -19.9 W m^{-2} (N=450, SD=1 W m^{-2}), -17.7 W m^{-2} (N=190, SD=0.7 W m^{-2}), -19.8 W m^{-2} (N=379, SD=1.2 W m^{-2}) and -14.6 W m^{-2} (N=450, SD=1 W m^{-2})for ERA5, LSA SAF, GLDAS and GLEAM comparison, respectively. Trend values are between -0.47 W m^{-2} dec^{-1} (GLDAS) and 0.564 W m^{-2} dec^{-1} (ERA5). Slope for ERA5 is higher from 2010 while higher values is observed for GLDAS before 1990. Excellent stability is observed with the LSA SAF dataset (no significative trend) and GLEAM (0.208 W m^{-2} dec^{-1}). No specific break is observed at the transition of each satellite. The maximum difference between mean values calculated over the time period covered by two successive instruments is 1.1 W m^{-2}.

C.2. Sensible heat flux

Figure 14 displays the monthly mean deseasonalized bias, averaged over the full disk, between CM SAF and ERA5, GLDAS and LSA SAF sensible heat flux values. Trend values are between -2.65 W m^{-2} dec^{-1} (ERA5) and 1.22 W m^{-2} dec^{-1} (LSA SAF). Values estimated over the MFG period are higher and less stable than estimations over the MSG period. For instance, for comparison with ERA5 dataset, which covers the longest period, the mean value is of 9.7 W m^{-2} (N=260, SD=1.7 W m^{-2}) for MFG period while it is of 3.2 W m^{-2} (N=190, SD=1.1 W m^{-2}) for MSG period. The maximum difference between mean values calculated over time covered by two successive instruments is of 3.8 W m^{-2} during MFG period (between Met-3 and Met-4) and 0.5 W m^{-2} for MSG period. In addition, a decrease of 6.4 W m^{-2} at MFG/MSG transition (between Met-7 and Met-8) is observed.

Stability clearly differ according to Europe, North Africa, South Africa and South America regions (Figures 15 and 16). First, over the full period, deseasonalized bias is higher in the South Africa region (on average 18 W m^{-2}) than the rest of the world (average around 6 W m^{-2}). Second, an important distinction can be made between MFG and MSG for all regions except Europe. Indeed, difference between averaged values over MFG and MSG period is of 9.5 W m^{-2}, 5.6 W m^{-2} and 7.4 W m^{-2} over North Africa, South Africa and South America regions,

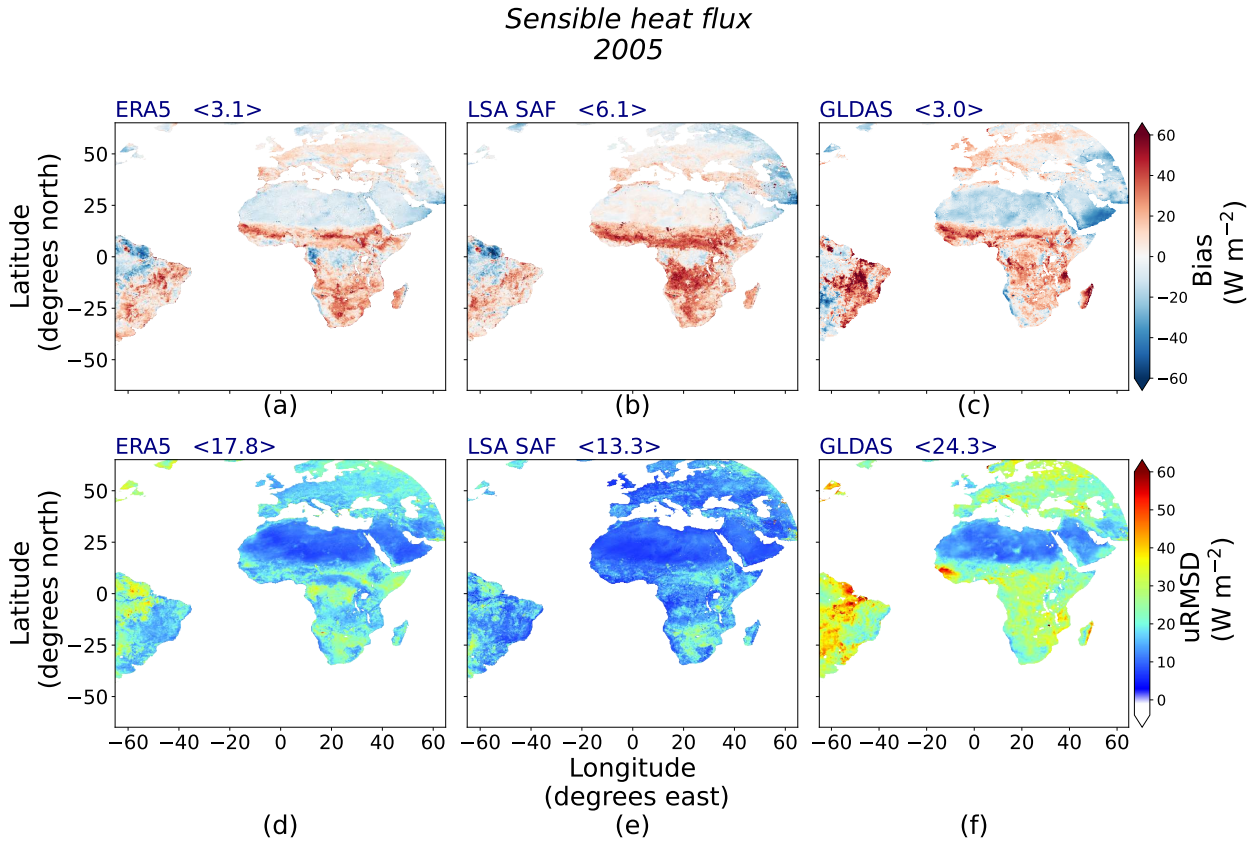

Fig. 12. Same as Fig. 10 but for sensible heat flux (W m^{-2}).

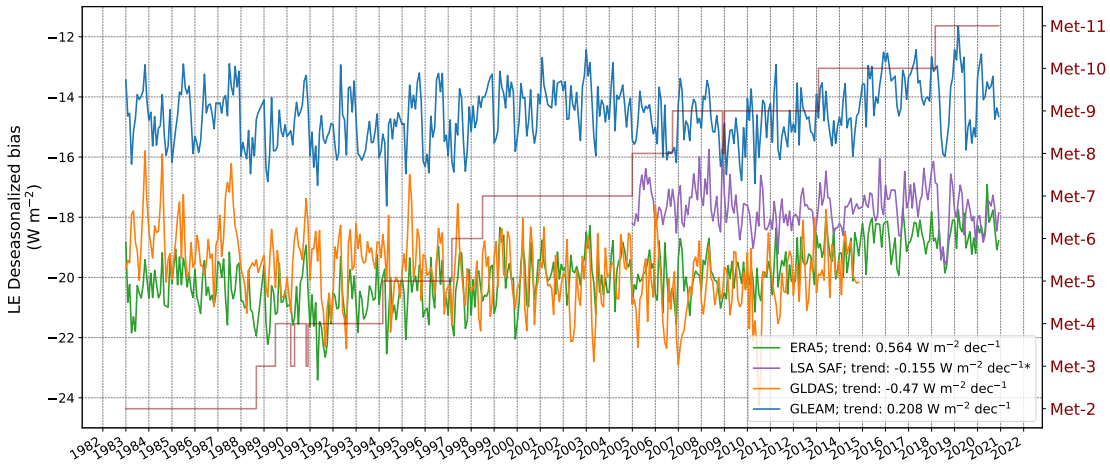

Fig. 13. Time series of deseasonalized bias (W m^{-2}) of monthly global latent heat flux compared to ERA5 (green), LSA SAF (violet), GLDAS (orange) and GLEAM (blue). Right axis indicates which Meteosat satellite is used (dark-red line). Trends (W m^{-2} dec^{-1}) are indicated in the legend and an (*) is added is the slope to calculate the trend is not significative (p-value > 0.05).

respectively, while it is of 2 W m^{-2} over Europe. Specific pattern can be noticed during Met-2 over the South America region (Fig. 16) with peaks of high values (> 20 W m^{-2}) as compared to mean value (12.7 W m^{-2}, SD of 3.4 W m^{-2}). Finally, considering MFG and MSG period separately, values for Africa regions are more stable than values obtained for the Europe and South America regions. For MFG period, the standard deviation is on average 2.2 W.m^{-2} for Africa regions while it is 2.3 W.m^{-2} for Euro/SAme. Similarly, for the MSG period, the standard deviation is on average 1.9 W.m^{-2} for Africa regions while it is 2.8 W.m^{-2} for Europe and South America.

The variations in the sensible heat flux are mainly due to instability in the surface incoming shortwave and the surface albedo which are, respectively, negatively and positively correlated to the sensible heat flux. Similar breaks are observed in the monthly mean deseasonalized bias as compared to ERA5 dataset for those two variables (Figures 17 and 18). In addition, analysis performed over different regions showed similar trends

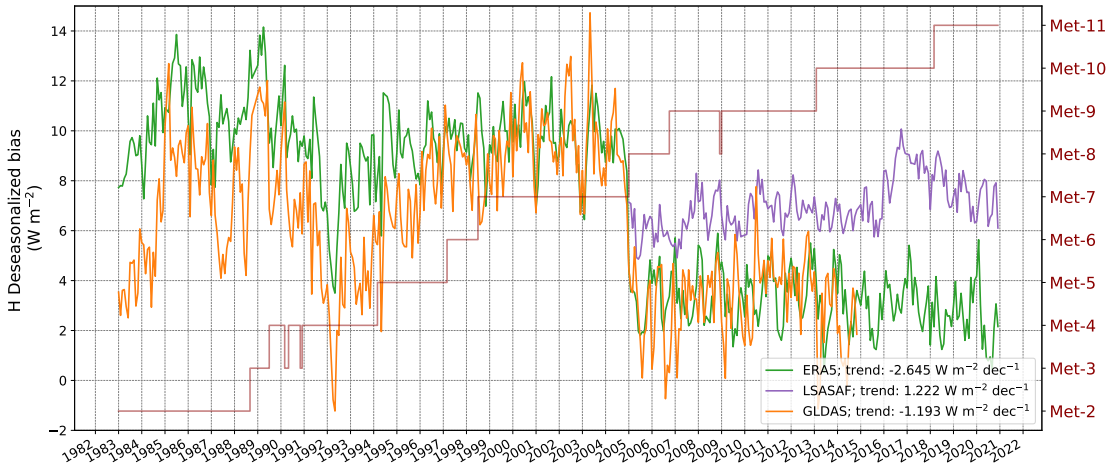

Fig. 14. Same as Fig. 13 but for sensible heat flux (W m^{-2}).

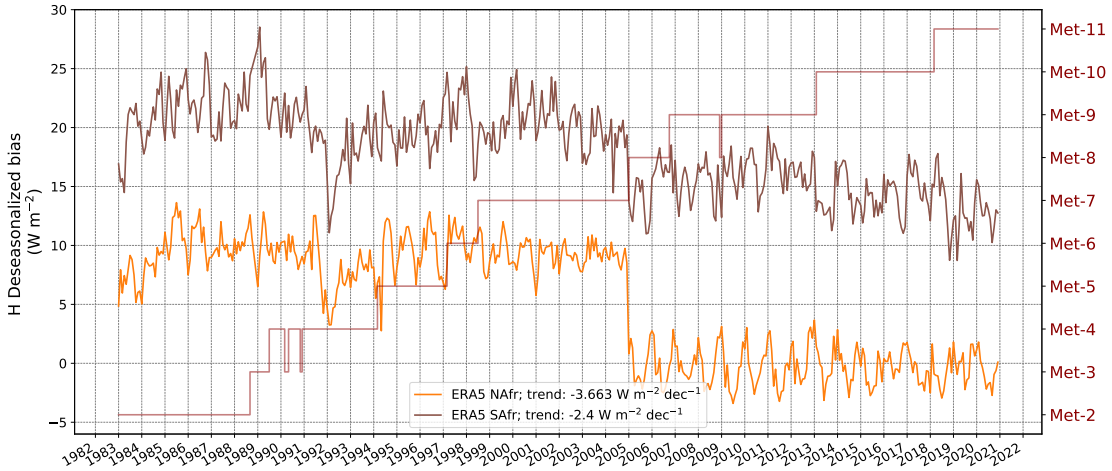

Fig. 15. Time series of deseasonalized bias (W m^{-2}) of the monthly sensible heat flux compared to ERA5 averaged over North Africa (yellow line) and South Africa (brown line) regions. Right axis indicates which Meteosat satellite is used (dark-red line). Trends values (W m^{-2} dec^{-1}) are indicated in the legend.

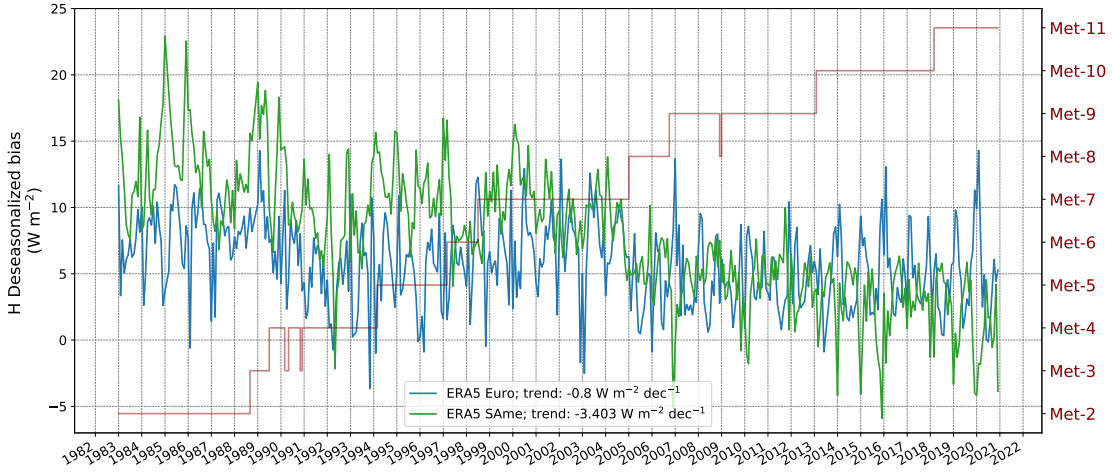

Fig. 16. Time series of deseasonalized bias (W m^{-2}) of the monthly sensible heat flux compared to ERA5 averaged over Europe (blue) and South America (green) regions. Right axis indicates which Meteosat satellite is used (dark-red). Trends values (W m^{-2} dec^{-1}) are indicated in the legend.

than the ones observed for the sensible heat flux (results not show here). Variations between MFG and MSG periods can be related to the narrow band to broad band relation used to derive variables over sand areas (see [38]). This latter would explain why the latent heat flux is not impacted as almost all energy goes to the sensible heat flux in such arid regions. Of course, sensor degradations and/or inter-calibration can still impact the results.

4. CONCLUSION

This study has presented the latent and sensible heat flux climate data record committed by the Satellite Application Facility on Climate Monitoring of EUMETSAT. The LE/H data record covers area up to 65°N/S and 65°W/E and consists in hourly, daily and monthly means with a spatial resolution of 0.05 degree over a period of almost 40 years (1983-2020). Those characteristics allow an unique combination of high spatial (0.05°) and temporal (hourly) resolutions for such covered time period 38 years. This particularity allows regional climate analysis and analyse multi-decadal variations. The Meteosat field of view covers a large domain of the globe centered around a longitude of 0° allows analysis over Europe, Africa, part of South America. Thus, this dataset would be highly complementary with other global dataset with lower spatial and/or temporal resolution or covering lower time period (e.g. GLEAM, ERA5, LSA SAF). For instance, for LSA SAF users, LSA SAF and CM SAF dataset being stable over MSG period for the latent heat flux (no significative trend in the stability), CM SAF dataset is a perfect complement to carry on analysis over MFG period.

Both products (LE and H) have been successfully validated against reference data records from observation sources (30 stations from FLUXNET2015 and ICOS networks), reanalysis (ERA5 and GLDAS) and satellite-based product (LSA SAF and GLEAM) and state of-the-art literature. Overall, when comparing with eddy covariance data, bias were of -9.7 (-10.8, -12.32) W m^{-2} for hourly (daily, monthly) latent heat flux and 1 (-2.6, -2.8) W m^{-2} for sensible heat flux. The unbiased root mean square difference was found to be 32.5 (24.7, 19.7) W m^{-2} for hourly (daily, monthly) latent heat flux, and 48.5 (34.1, 23.6) W m^{-2} for sensible heat flux. Same order of magnitude have been observed for other products and in the literature. Note that higher errors have been obtained for high values cases (day time). Grid based comparisons, carried out over the full disk for the year 2005 showed and underestimation of LE and larger discrepancies in the Southern regions (latitude lower than 16°N). The LE product is stable with, for instance, no significative trend in monthly mean deseasonalized bias as compared to LSA SAF product. H product is really stable over Europe but limitations are noticed over the rest of the world with a break at MFG/MSG transition. In the future, improvements will focus on : i) reduce global the underestimation of the latent heat flux by an adaptation of the source of soil moisture and/or land cover map, adaptation of the minimum stomatal resistance and/or change adapt the algorithm to improve the repartition of energy between LE, H and G for high values cases and ii) Reduce the instability for the sensible heat flux over sand areas.

In an ongoing study we plane to create a prototype based available satellite data to extend the product globaly. To do so, the mosaic of geostationary satellites, known as GEORING, would be harmonized and intercalibrated radiances in order to get produce necessary inputs.

This dataset will be available before the end of the year. The internet address http://wui.cmsaf.eu/ allows direct access to the CM SAF data ordering interface. On this webpage a detailed description how to use the interface for product search and ordering is given. We refer the user to this description since it is the central and most up to date documentation.

5. REFERENCES

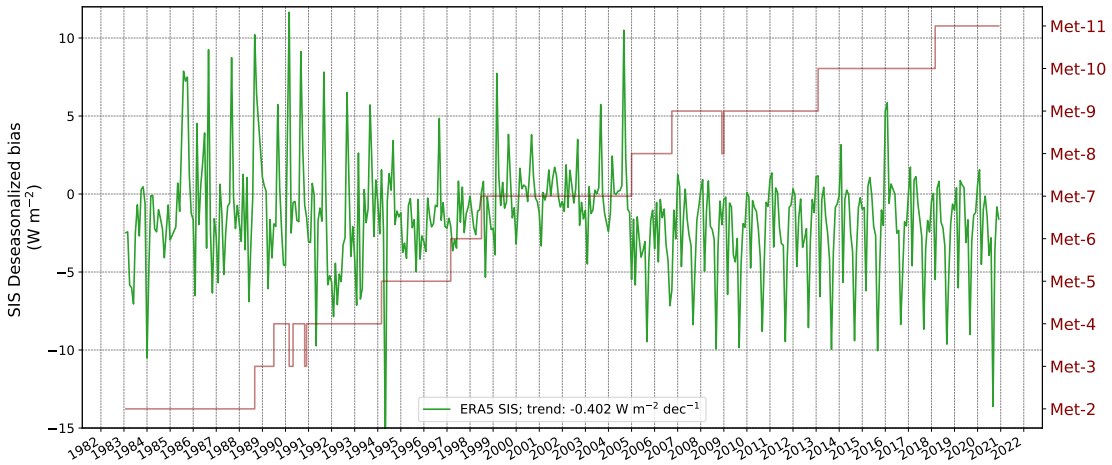

Fig. 17. Time series of deseasonalized bias (W m^{-2}) of the CM SAF monthly albedo flux as compared to ERA5 averaged over the full disk. The red line represents the delimitations between Meteosat satellite used. The trend values (W m^{-2} dec^{-1}) of the time series is indicated in the legend.

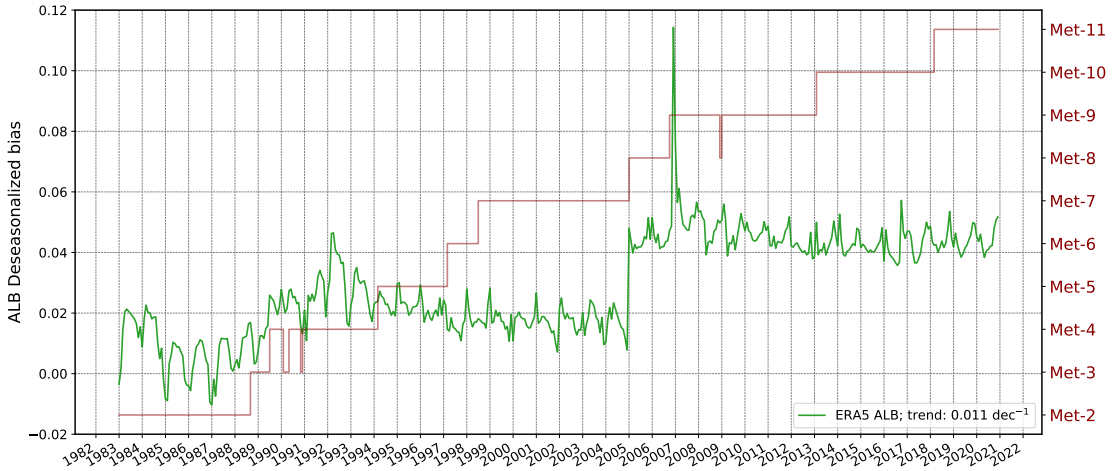

Fig. 18. Same as Fig. 17 but for the surface incoming shortwave radiation.

FULL REFERENCES

1. R. Pipunic, J. Walker, and A. Western, "Assimilation of remotely sensed data for improved latent and sensible heat flux prediction: A comparative synthetic study," Remote. Sens. Environ. **112**, 1295–1305 (2008).
2. C. Mito, R. Boiyo, and G. Laneve, "A simple algorithm to estimate sensible heat flux from remotely sensed modis data," Int. journal remote sensing **33**, 6109–6121 (2012).
3. G. G. Katul, R. Oren, S. Manzoni, C. Higgins, and M. B. Parlange, "Evapotranspiration: a process driving mass transport and energy exchange in the soil-plant-atmosphere-climate system," Rev. Geophys. **50** (2012).
4. D. Michel, C. Jiménez, D. G. Miralles, M. Jung, M. Hirschi, A. Ershadi, B. Martens, M. F. McCabe, J. B. Fisher, Q. Mu *et al.*, "The wacmos-et project–part 1: Tower-scale evaluation of four remote-sensing-based evapotranspiration algorithms," Hydrol. Earth Syst. Sci. **20**, 803–822 (2016).
5. A. Behrendt, V. Wulfmeyer, C. Senff, S. K. Muppa, F. Späth, D. Lange, N. Kalthoff, and A. Wieser, "Observation of sensible and latent heat flux profiles with lidar," Atmospheric Meas. Tech. **13**, 3221–3233 (2020).
6. T. Oki and S. Kanae, "Global hydrological cycles and world water resources," science **313**, 1068–1072 (2006).
7. P. Sellers, R. Dickinson, D. Randall, A. Betts, F. Hall, J. Berry, G. Collatz, A. Denning, H. Mooney, C. Nobre *et al.*, "Modeling the exchanges of energy, water, and carbon between continents and the atmosphere," Science **275**, 502–509 (1997).
8. K. E. Trenberth, J. T. Fasullo, and J. Kiehl, "Earth's global energy budget," Bull. Am. Meteorol. Soc. **90**, 311–324 (2009).
9. Y.-A. Liou and S. K. Kar, "Evapotranspiration estimation with remote sensing and various surface energy balance algorithms—a review," Energies **7**, 2821–2849 (2014).
10. J. B. Fisher, F. Melton, E. Middleton, C. Hain, M. Anderson, R. Allen, M. F. Mccabe, S. Hook, D. Baldocchi, P. A. Townsend, A. Kilic, K. Tu, D. Miralles, J. Perret, J.-P. Lagouarde, D. Waliser, A. J. Purdy, A. French, D. Schimel, J. S. Famiglietti, G. Stephens, and E. F. Wood, "The future of evapotranspiration: Global requirements for ecosystem functioning, carbon and climate feedbacks, agricultural management, and water resources," Water Resour. Res. **10.1002/20**, 2618–2626 (2017).
11. K. Yang, J. Qin, X. Guo, D. Zhou, and Y. Ma, "Method development for estimating sensible heat flux over the tibetan plateau from cma data," J. Appl. Meteorol. Climatol. **48**, 2474–2486 (2009).
12. H. Wang and D. Li, "Correlation of surface sensible heat flux in the arid region of northwestern china with the northern boundary of the east asian summer monsoon and chinese summer precipitation," J. Geophys. Res. Atmospheres **116**, 1–15 (2011).
13. N. Shan, Z. Shi, X. Yang, X. Zhang, H. Guo, B. Zhang, and Z. Zhang, "Trends in potential evapotranspiration from 1960 to 2013 for a desertification-prone region of china," Int. J. Climatol. **36**, 3434–3445 (2016).
14. H. Hersbach, B. Bell, P. Berrisford, G. Biavati, D. Dee, A. Horányi, J. Nicolas, C. Peubey, R. Radu, I. Rozum *et al.*, "The era5 global atmospheric reanalysis at ecmwf as a comprehensive dataset for climate data homogenization, climate variability, trends and extremes." in *Geophysical Research Abstracts,* vol. 21 (2019).
15. R. R. Gillies, T. N. Carlson, J. Cui, W. P. Kustas, and K. S. Hume, "A verification of the ″triangle″ method for obtaining surface soil water content and energy fluxes from remote measurements of the normalized diverence vegetation index (ndvi) and surface radiant temperature," Remote. Sens. **18**, 3145–3166 (1997).
16. C. Watts, A. Chehbouni, J.-C. Rodriguez, Y. Kerr, O. Hartogensis, and H. De Bruin, "Comparison of sensible heat flux estimates using avhrr with scintillometer measurements over semi-arid grassland in northwest mexico," Agric. For. Meteorol. **105**, 81–89 (2000).
17. L. Jiang and S. Islam, "Estimation of surface evaporation map over southern great plains using remote sensing data," Water Resour. Res. **37**, 329–340 (2001).
18. L. Jiang and S. Islam, "An intercomparison of regional latent heat flux estimation using remote sensing data," Int. J. Remote. Sens. **24**, 2221–2236 (2003).
19. L. Jiang, S. Islam, and T. N. Carlson, "Uncertainties in latent heat flux measurement and estimation: Implications for using a simplified approach with remote sensing data," Can. J. Remote. Sens. **30**, 769–787 (2004).
20. F. Caparrini, F. Castelli, and D. Entekhabi, "Estimation of surface turbulent fluxes through assimilation of radiometric surface temperature sequences," J. Hydrometeorol. **5**, 145–159 (2004).
21. N. Batra, S. Islam, V. Venturini, G. Bisht, and L. Jiang, "Estimation and comparison of evapotranspiration from modis and avhrr sensors for clear sky days over the southern great plains," Remote. Sens. Environ. **103**, 1–15 (2006).
22. H. Su, E. F. Wood, M. F. Mccabe, and Z. Su, "Evaluation of remotely sensed evapotranspiration over the ceop eop-1 reference sites," J. Meteorol. Soc. Jpn. **85**, 439–459 (2007).
23. T. F. Foken, "The energy balance closure problem : an overview," Ecol. Appl. **18**, 1351–1367 (2008).
24. J. D. Kalma, T. R. McVicar, and M. F. McCabe, "Estimating land surface evaporation: A review of methods using remotely sensed surface temperature data," Surv. Geophys. **29**, 421–469 (2008).
25. S. Stisen, I. Sandholt, A. Nørgaard, R. Fensholt, and K. H. Jensen, "Combining the triangle method with thermal inertia to estimate regional evapotranspiration - applied to msg-seviri data in the senegal river basin," Remote. Sens. Environ. **112**, 1242–1255 (2008).

26. W. W. Verstraeten, F. Veroustraete, and J. Feyen, "Assessment of evapotranspiration and soil moisture content across different scales of observation," Sensors **8**, 70–117 (2008).
27. M. C. Anderson, R. G. Allen, A. Morse, and W. P. Kustas, "Use of landsat thermal imagery in monitoring evapotranspiration and managing water resources," Remote. Sens. Environ. **122**, 50–65 (2012).
28. S.-H. Hong, J. M. Hendrickx, J. Kleissl, R. G. Allen, W. G. Bastiaanssen, R. L. Scott, and A. L. Steinwand, "Evaluation of an extreme-condition-inverse calibration remote sensing model for mapping energy balance fluxes in arid riparian areas," Hydrol. Earth Syst. Sci. Discuss. **11**, 13479–13539 (2014).
29. Y. Yang, D. Long, H. Guan, W. Liang, C. Simmons, and O. Batelaan, "Comparison of three dual-source remote sensing evapotranspiration models during the musoexe-12 campaign: Revisit of model physics," Water Resour. Res. pp. 3145–3165 (2015).
30. A. Loew, J. Peng, and M. Borsche, "High-resolution land surface fluxes from satellite and reanalysis data (holaps v1.0): Evaluation and uncertainty assessment," Geosci. Model. Dev. **9**, 2499–2532 (2016).
31. M. F. Mccabe, A. Ershadi, C. Jimenez, D. Miralles, D. Michel, and E. F. Wood, "The gewex landflux project: Evaluation of model evaporation using tower-based and globally gridded forcing data," Geosci. Model. Dev. **9**, 283–305 (2016).
32. Q. Zhuang, B. Wu, N. Yan, W. Zhu, and Q. Xing, "A method for sensible heat flux model parameterization based on radiometric surface temperature and environmental factors without involving the parameter kb- 1," Int. journal applied earth observation geoinformation **47**, 50–59 (2016).
33. N. Laounia, H. Abderrahmane, K. Abdelkader, S. Zahira, and Z. Mansour, "Evapotranspiration and surface energy fluxes estimation using the landsat-7 enhanced thematic mapper plus image over a semiarid agrosystem in the north-west of algeria," Revista Brasileira de Meteorol. **32**, 691–702 (2017).
34. F. Feng, X. Li, Y. Yao, and M. Liu, "Long-term spatial distributions and trends of the latent heat fluxes over the global cropland ecosystem using multiple satellite-based models," PLoS ONE **12**, 1–18 (2017).
35. D. G. Miralles, C. Jiménez, M. Jung, D. Michel, A. Ershadi, M. McCabe, M. Hirschi, B. Martens, A. J. Dolman, J. B. Fisher *et al.*, "The wacmos-et project–part 2: Evaluation of global terrestrial evaporation data sets," Hydrol. Earth Syst. Sci. **20**, 823–842 (2016).
36. N. Ghilain, A. Arboleda, and F. Gellens-Meulenberghs, "Evapotranspiration modelling at large scale using near-real time msg seviri derived data," Hydrol. Earth Syst. Sci. **15**, 771–786 (2011).
37. W. Moutier, A. Arboleda, M. Barrios, N. Ghilain, and N. Clerbaux, "Algorithm theoretical basis document meteosat latent and sensible heat fluxes," https://cmsaf.eu (2020).
38. Q. . Bourgeois, "Validation report surface radiative budget," https://cmsaf.eu (2023).
39. Y. Liu, R. Liu, and J. M. Chen, "Retrospective retrieval of long-term consistent global leaf area index (1981–2011) from combined avhrr and modis data," J. Geophys. Res. Biogeosciences **117** (2012).
40. Y. Liu, R. Liu, J. Pisek, and J. M. Chen, "Separating overstory and understory leaf area indices for global needleleaf and deciduous broadleaf forests by fusion of modis and misr data," Biogeosciences **14**, 1093–1110 (2017).
41. "Esa land cover cci product user guide version 2. tech. rep." https://maps.elie.ucl.ac.be/CCI/viewer/download/ESACCI-LC-Ph2-PUGv2_2.0.pdf (2020).
42. S. Bontemps, M. Herold, L. Kooistra, A. Van Groenestijn, A. Hartley, O. Arino, I. Moreau, and P. Defourny, "Revisiting land cover observation to address the needs of the climate modeling community," Biogeosciences **9**, 2145–2157 (2012).
43. M. Simard, N. Pinto, J. B. Fisher, and A. Baccini, "Mapping forest canopy height globally with spaceborne lidar," J. Geophys. Res. Biogeosciences **116** (2011).
44. N. Ghilain, A. Arboleda, G. Sepulcre-Cantò, O. Batelaan, J. Ardö, and F. Gellens-Meulenberghs, "Improving evapotranspiration in a land surface model using biophysical variables derived from msg/seviri satellite," Hydrol. Earth Syst. Sci. **16**, 2567–2583 (2012).
45. F. Gellens-Meulenberghs, A. Arboleda, and N. Ghilain, "Status of development of the lsa-saf evapotranspiration product," in *Proceedings of the 2nd LSA-SAF Training workshop, Lisbon,[8-10 March],* (2006).
46. F. Gellens-Meulenberghs, A. Arboleda, and N. Ghailain, "Towards a continuous monitoring of evapotranspiration based on msg data," IAHS PUBLICATION **316**, 228 (2007).
47. B. van den Hurk, P. Viterbo, A. Beljaars, and A. Betts, "O ine validation of the era40 surface scheme," Tech. rep., Citeseer (2000).
48. P. Viterbo and A. C. Beljaars, "An improved land surface parameterization scheme in the ecmwf model and its validation," J. climate **8**, 2716–2748 (1995).
49. G. Balsamo, A. Beljaars, K. Scipal, P. Viterbo, B. van den Hurk, M. Hirschi, and A. K. Betts, "A revised hydrology for the ecmwf model: Verification from field site to terrestrial water storage and impact in the integrated forecast system," J. hydrometeorology **10**, 623–643 (2009).
50. Y. Y. Liu, R. Parinussa, W. A. Dorigo, R. A. De Jeu, W. Wagner, A. Van Dijk, M. F. McCabe, and J. Evans, "Developing an improved soil moisture dataset by blending passive and active microwave satellite-based retrievals," Hydrol. Earth Syst. Sci. **15**, 425–436 (2011).
51. G. Pastorello, C. Trotta, E. Canfora, H. Chu, D. Christianson, Y.-W. Cheah, C. Poindexter, J. Chen, A. Elbashandy, M. Humphrey *et al.*, "The fluxnet2015 dataset and the oneflux processing pipeline for eddy covariance data," Sci. data **7**, 1–27 (2020).
52. B. Rodell, P. Houser, U. Jambor, J. Gottschalck, K. Mitchell, C. Meng, K. Arsenault, B. Cosgrove, J. Radakovich, M. Bosilovich *et al.*, "The global land data assimilation system this powerful new land surface modeling system integrates data from advanced observing systems to support improved forecast model initialization and hydrometeorological investigations, b. am. meteorol. soc., 85, 381–394," (2004).
53. D. G. Miralles, T. R. Holmes, R. A. De Jeu, J. H. Gash, A. G. Meesters, and A. J. Dolman, "Global land-surface evaporation estimated from satellite-based observations," Hydrol. Earth Syst. Sci. **15**, 453–469 (2011).
54. B. Martens, D. G. Miralles, H. Lievens, R. Van Der Schalie, R. A. De Jeu, D. Fernández-Prieto, H. E. Beck, W. A. Dorigo, and N. E. Verhoest, "Gleam v3: Satellite-based land evaporation and root-zone soil moisture," Geosci. Model. Dev. **10**, 1903–1925 (2017).
55. C. Rebmann, M. Göckede, T. Foken, M. Aubinet, M. Aurela, P. Berbigier, C. Bernhofer, N. Buchmann, A. Carrara, A. Cescatti *et al.*, "Quality analysis applied on eddy covariance measurements at complex forest sites using footprint modelling," Theor. Appl. Climatol. **80**, 121–141 (2005).
56. M. Reichstein, E. Falge, D. Baldocchi, D. Papale, M. Aubinet, P. Berbigier, C. Bernhofer, N. Buchmann, T. Gilmanov, A. Granier *et al.*, "On the separation of net ecosystem exchange into assimilation and ecosystem respiration: review and improved algorithm," Glob. change biology **11**, 1424–1439 (2005).
57. K. Wilson and Others, "Energy balance closure at fluxnet sites," Agric. For. Meteorol. **113**, 223–243 (2002).
58. H. H. Franssen, R. Stöckli, I. Lehner, E. Rotenberg, and S. I. Seneviratne, "Energy balance closure of eddy-covariance data: A multisite analysis for european fluxnet stations," Agric. For. Meteorol. **150**, 1553–1567 (2010).
59. P. C. Stoy, M. Mauder, T. Foken, B. Marcolla, E. Boegh, A. Ibrom, M. A. Arain, A. Arneth, M. Aurela, C. Bernhofer *et al.*, "A data-driven analysis of energy balance closure across fluxnet research sites: The role of landscape scale heterogeneity," Agric. forest meteorology **171**, 137–152 (2013).
60. G. B. Senay, S. Kagone, and N. M. Velpuri, "Operational global actual evapotranspiration: Development, evaluation, and dissemination," Sensors **20**, 1915 (2020).
61. I. S. Bowen, "The ratio of heat losses by conduction and by evaporation from any water surface," Phys. review **27**, 779 (1926).
62. A. Chehbouni, Y. Kerr, C. Watts, O. Hartogensis, D. Goodrich, R. Scott, J. Schieldge, K. Lee, W. Shuttleworth, G. Dedieu *et al.*, "Estimation of area-average sensible heat flux using a large-aperture scintillometer during the semi-arid land-surface-atmosphere (salsa) experiment," Water Resour. Res. **35**, 2505–2511 (1999).

63. J. Z. Drexler, R. L. Snyder, D. Spano, and K. T. Paw U, "A review of models and micrometeorological methods used to estimate wetland evapotranspiration," Hydrol. Process. **18**, 2071–2101 (2004).
64. J. L. Chávez, T. A. Howell, and K. S. Copeland, "Evaluating eddy covariance cotton et measurements in an advective environment with large weighing lysimeters," Irrigation Sci. **28**, 35–50 (2009).
65. D. L. McJannet, F. J. Cook, R. P. McGloin, H. A. McGowan, and S. Burn, "Estimation of evaporation and sensible heat flux from open water using a large-aperture scintillometer," Water Resour. Res. **47**, 1–14 (2011).
66. O. Perez-Priego, T. S. El-Madany, M. Migliavacca, A. S. Kowalski, M. Jung, A. Carrara, O. Kolle, M. P. Martín, J. Pacheco-Labrador, G. Moreno *et al.*, "Evaluation of eddy covariance latent heat fluxes with independent lysimeter and sapflow estimates in a mediterranean savannah ecosystem," Agric. For. Meteorol. **236**, 87–99 (2017).
67. M. Hirschi, D. Michel, I. Lehner, and S. I. Seneviratne, "A site-level comparison of lysimeter and eddy covariance flux measurements of evapotranspiration," Hydrol. Earth Syst. Sci. **21**, 1809–1825 (2017).
68. G. Balsamo, C. Albergel, A. Beljaars, S. Boussetta, E. Brun, H. Cloke, D. Dee, E. Dutra, J. Muñoz-Sabater, F. Pappenberger *et al.*, "Era-interim/land: a global land surface reanalysis data set," Hydrol. Earth Syst. Sci. **19**, 389–407 (2015).
69. C. Albergel, G. Balsamo, P. De Rosnay, J. Muñoz-Sabater, and S. Boussetta, "A bare ground evaporation revision in the ecmwf land-surface scheme: evaluation of its impact using ground soil moisture and satellite microwave data," Hydrol. Earth Syst. Sci. **16**, 3607–3620 (2012).
70. B. Martens, D. L. Schumacher, H. Wouters, J. Muñoz-Sabater, N. E. Verhoest, and D. G. Miralles, "Evaluating the land-surface energy partitioning in era5," Geosci. Model. Dev. **13**, 4159–4181 (2020).
71. S. V. Kumar, C. D. Peters-Lidard, Y. Tian, P. R. Houser, J. Geiger, S. Olden, L. Lighty, J. L. Eastman, B. Doty, P. Dirmeyer *et al.*, "Land information system: An interoperable framework for high resolution land surface modeling," Environ. modelling & software **21**, 1402–1415 (2006).
72. J. Sheffield, G. Goteti, and E. F. Wood, "Development of a 50-year high-resolution global dataset of meteorological forcings for land surface modeling," J. climate **19**, 3088–3111 (2006).
73. F. Chen, K. Mitchell, J. Schaake, Y. Xue, H.-L. Pan, V. Koren, Q. Y. Duan, M. Ek, and A. Betts, "Modeling of land surface evaporation by four schemes and comparison with fife observations," J. Geophys. Res. Atmospheres **101**, 7251–7268 (1996).
74. M. Ek, K. Mitchell, Y. Lin, E. Rogers, P. Grunmann, V. Koren, G. Gayno, and J. Tarpley, "Implementation of noah land surface model advances in the national centers for environmental prediction operational mesoscale eta model," J. Geophys. Res. Atmospheres **108** (2003).
75. D. G. Miralles, J. H. Gash, T. R. Holmes, R. A. de Jeu, and A. Dolman, "Global canopy interception from satellite observations," J. Geophys. Res. Atmospheres **115** (2010).
76. C. H. B. Priestley and R. J. Taylor, "On the assessment of surface heat flux and evaporation using large-scale parameters," Mon. weather review **100**, 81–92 (1972).
77. X. Zhang, Y. Dai, H. Cui, R. E. Dickinson, S. Zhu, N. Wei, B. Yan, H. Yuan, W. Shangguan, L. Wang *et al.*, "Evaluating common land model energy fluxes using fluxnet data," Adv. atmospheric Sci. **34**, 1035–1046 (2017).
78. C. Albergel, S. Munier, A. Bocher, B. Bonan, Y. Zheng, C. Draper, D. J. Leroux, and J.-C. Calvet, "Ldas-monde sequential assimilation of satellite derived observations applied to the contiguous us: An era-5 driven reanalysis of the land surface variables," Remote. Sens. **10**, 1627 (2018).
79. J. Peng, S. Kharbouche, J.-P. Muller, O. Danne, S. Blessing, R. Giering, N. Gobron, R. Ludwig, B. Müller, G. Leng *et al.*, "Influences of leaf area index and albedo on estimating energy fluxes with holaps framework," J. Hydrol. **580**, 124245 (2020).
80. X. Guo, D. Meng, X. Chen, and X. Li, "Validation and comparison of seven land surface evapotranspiration products in the haihe river basin, china," Remote. Sens. **14**, 4308 (2022).
81. Y. Xin, J. Liu, X. Liu, G. Liu, X. Cheng, and Y. Chen, "Reduction of uncertainties in surface heat flux over the tibetan plateau from era-interim to era5," Int. J. Climatol. **42**, 6277–6292 (2022).
82. A. L. Siemann, N. Chaney, and E. F. Wood, "Development and validation of a long-term, global, terrestrial sensible heat flux dataset," J. Clim. **31**, 6073–6095 (2018).
83. P. Viterbo, A. Beljaars, J.-F. Mahfouf, and J. Teixeira, "The representation of soil moisture freezing and its impact on the stable boundary layer," Q. J. Royal Meteorol. Soc. **125**, 2401–2426 (1999).
84. N. . i. I. DOCUMENTATION-Cy31r1, "Ecmwf part iv: physical processes," . pp. 1261–1982 (2017).
85. M. T. Van Genuchten, "A closed-form equation for predicting the hydraulic conductivity of unsaturated soils," Soil science society Am. journal **44**, 892–898 (1980).
86. R. B. Clapp and G. M. Hornberger, "Empirical equations for some soil hydraulic properties," Water resources research **14**, 601–604 (1978).
87. B. Choudhury, S. Idso, and R. Reginato, "Analysis of an empirical model for soil heat flux under a growing wheat crop for estimating evaporation by an infrared-temperature based energy balance equation," Agric. For. Meteorol. **39**, 283–297 (1987).
88. W. G. M. Bastiaanssen, *Regionalization of surface flux densities and moisture indicators in composite terrain: A remote sensing approach under clear skies in Mediterranean climates* (Wageningen University and Research, 1995).
89. J. M. Norman, W. P. Kustas, and K. S. Humes, "Source approach for estimating soil and vegetation energy fluxes in observations of directional radiometric surface temperature," Agric. For. Meteorol. **77**, 263–293 (1995).
90. A. Chehbouni, D. L. Seen, E. Njoku, and B. Monteny, "Examination of the difference between radiative and aerodynamic surface temperatures over sparsely vegetated surfaces," Remote. Sens. Environ. **58**, 177–186 (1996).
91. A. Jacobsen, "Estimation of the soil heat flux/net radiation ratio based on spectral vegetation indexes in high-latitude arctic areas," Int. J. Remote. Sens. **20**, 445–461 (1999).
92. M. A. Friedl, "Forward and inverse modeling of land surface energy balance using surface temperature measurements," Remote. sensing environment **79**, 344–354 (2002).
93. W. P. Kustas, C. S. Daughtry, and P. J. Van Oevelen, "Analytical treatment of the relationships between soil heat flux/net radiation ratio and vegetation indices," Remote. sensing environment **46**, 319–330 (1993).
94. Z. Su, "The surface energy balance system (sebs) for estimation of turbulent heat fluxes," Hydrol. earth system sciences **6**, 85–100 (2002).
95. J. A. Santanello Jr and M. A. Friedl, "Diurnal covariation in soil heat flux and net radiation," J. Appl. Meteorol. **42**, 851–862 (2003).
96. A. C. Beljaars and P. Viterbo, "The sensitivity of winter evaporation to the formulation of aerodynamic resistance in the ecmwf model," Boundary-Layer Meteorol. **71**, 135–149 (1994).
97. V. Masson, J. L. Champeaux, F. Chauvin, C. Meriguet, and R. Lacaze, "A global database of land surface parameters at 1-km resolution in meteorological and climate models," J. Clim. **16**, 1261–1982 (2003).

Appendices

A. MODEL DESCRIPTION

A. Meteorological data processing

A.1. Total wind speed

The vector average wind speed at 10 meters is calculated as:

$$U_a = \sqrt{U^2 + V^2} \tag{11}$$

with, U and V, the component vector winds at 10 meters.

A.2. Topographic correction for temperatures

The general equation to apply topographic correction for 2 metres air temperature (T_a) and 2 metres dew point temperature (T_{2d}) is defined as following:

$$T_{\text{cor}} = T_{\text{uncor}} + (\gamma \times \left(DEM - \frac{z}{g} \right)) \quad (12)$$

where, is the reference lapse rate (-0.0067 K m^{-1}), g is the gravitational acceleration (9.8 m s^{-2}), z the geopotential and DEM the altitude from the digital elevation model. In the following, T_a and T_{2d} would refer to the corrected values.

A.3. Relative humidity

The Relative humidity (Rh, unitless) is the ratio between the saturation vapor pressure of T_{2d} and T_a:

$$Rh = \frac{e_w(T_{2d})}{e_w(T_a)} \quad (13)$$

with,

$$e_w(T) = 100 \times 6.112 \times \exp\left(\frac{17.62 \times T}{243.12 + T} \right) \quad (14)$$

where T is the temperature (T_{2d} or T_a) in degree Celsius and e_w is the vapor pressure at saturation in Pa (Guide To Meteorological Instruments And Methods Of Observation, 2018).

A.4. Soil moisture

For each tile composing the pixel, the soil moisture is obtained by averaging the volumetric soil content at four soil layers weighted by the root density per layer, as indicated in the following:

$$\bar{\theta} = R_k \times \max\left(f_{liq,k} \times \text{swvl}_k \times \theta_{\text{pwp}} \right) \quad (15)$$

R_k is root density (Table 5), the permanent wilting point (see Table 6), *swvl* the volumetric soil water of the k^{th} layer and $f_{liq,k}$ (Figure 2) the fraction of unfrozen soil water [83, 84] where the formulation depends on the soil temperature of the k^{th} layer (slt_k).

if $slt_k > T_{f1}$ (= 274.15 K):

$$f_{liq,k} = 1 \quad (16)$$

if $slt_k < T_{f2}$ (= 270.15 K):

$$f_{liq,k} = 0 \quad (17)$$

if $T_{f2} \leq slt_k \leq T_{f1}$:

$$f_{liq,k} = 1 - 0.05 \times \left\{ 1 - sin\left[\frac{\pi \times \left(\text{slt}_k - 0.5 \times T_{f1} - 0.5 \times T_{f2} \right)}{T_{f1} - T_{f2}} \right] \right\} \quad (18)$$

While it could be calculated hourly, the daily mean will be used to be consistent with the (daily) soil moisture retrieved by satellite. Thus, the inputs in the Eq. 15 and 18 are daily averaged values.

B. Model description at the tile level

B.1. The surface energy balance

The algorithm is an energy balance model aiming to partition the available energy between *LE*, *H* and heat conduction flux into the ground (*G*). Thus, for each tile, a closure of the surface energy budget is obtained. The surface energy balance is computed by the algorithm at tile level in a conceptual layer, called skin layer. This latter represents the coverage of the land as a flat layer, without description of the 3-D structure of the canopy. At the tile level i^{th}, the global surface energy balance equation can be written as:

$$R_{\text{Ni}} = H_i + \text{LE}_i + G_i \quad (19)$$

Table 5. Minimum stomatal resistance (rs_{min}, s m^{-1}) and root density distribution (R_k) per vegetation type (in %) over the four layers.

Surface type (number)	rs_{min}	R_1	R_2	R_3	R_4
Bare soil (1)	250	100	0	0	0
Snow (2)	-	-	-	-	-
Deciduous Broadleaved trees (3)	350	24	38	31	7
Evergreen Needleleaved trees (4)	180	26	39	29	6
Evergreen Broadleaved trees (5)	200	25	34	27	14
Crops (6)	180	24	41	31	4
Irrigated crops (7)	180	24	41	31	4
Grass (8)	110	35	38	23	4
Bogs and Marshes (9)	250	25	34	27	11
Rocks (10)	1000	-	-	-	-
Inland water (11)	0	-	-	-	-
City (12)	1000	-	-	-	

Table 6. Values for the volumetric soil moisture in Van Genuchten (1980) [85] and Clapp-Hornberger (1978) [86], field capacity, θ_{fc} and permanent wilting point, θ_{pwp} ($m^3 m^{-3}$) that are used in ERA5 (table extracted from [84]).

Soil type (texture)	θ_{pwp}	θ_{fc}
Coarse	0.059	0.244
Medium	0.151	0.347
Medium-Fine	0.133	0.383
Fine	0.279	0.448
Very Fine	0.335	0.541
Organic	0.267	0.663
Loamy (CH)	0.171	0.323

with,

$$R_{\text{Ni}} = (1 - SAL) \times SIS + \varepsilon \times \left(SDL - \sigma T_{sk,i}^4 \right) \quad (20)$$

where, $R_{Ni,}$ *SIS*, *SDL*, $T_{sk,i}$, , σ and stand, respectively, for the net radiation, the Surface Incoming Shortwave radiation, the Surface Downward Longwave radiation, the skin temperature of the i^{th} tile, the surface albedo, the Stefan-Boltzmann constant (=5.67 10^{-8} W m^{-2} K^{-4}) and the surface emissivity.

To have typically positive fluxes, at least during day time, the following sign conventions are adopted:

- R_{Ni} is the difference between incoming and outgoing radiation at the surface (SW+LW). A positive value means there is a net absorption of radiant energy in the skin layer.
- The heat H, LE and G are positive when the energy leaves the skin layer toward the atmosphere (H, LE) or the ground (G).
- The SIS and SDL radiative fluxes incident at the surface are always positive

B.2. The Heat flux conduction into the ground

A common choice to parameterize the soil heat flux (G_i) is to approximate it as a fraction (β_i) of the net surface radiation (R_{Ni},) assuming that it has a diurnal variation in phase with the net radiation. While different variants based on the same assumption exist in the literature [87–95], we choose the parameterization of Chehbouni et al., (1996), and is adapted for specific land types. Thus, G_i is defined as following:

$$G_i = \beta_i \times R_{\mathrm{Ni}} \tag{21}$$

with, β_i equal to 0.4 for city surface type, 0.2 for rock and bare soil tile, 0.05 for snow tile. Concerning other tiles, β_i is equal to 0.1 for R_{Ni} >0 and 0.4 for R_{Ni} *le* 0 cases.

B.3. Latent and Sensible heat flux

The latent and sensible heat fluxes are obtained via a resistance approach, combining a response of the stomata closure by environmental stress (canopy resistance to transpiration) and the aerodynamic resistance:

$$\mathrm{LE}_i = \frac{L_v \rho_a}{(r_{a_i} + r_{c_i})} \left[q_{\mathrm{sat}} \left(T_{sk,i} \right) - q_a(T_a) \right] \tag{22}$$

and

$$H_i = \frac{\rho_a}{r_{a_i}} \left[c_p (T_{sk,i} - T_a) - g z_a \right] \tag{23}$$

where:

- L_v is the latent heat of vaporization (J kg^{-1}),
- ρ_a is the air density (kg m^{-3}),
- q_a, is the specific humidity (kg kg^{-1}) at air temperature T_a (2m above the surface, in K),
- q_{sat}, is the specific humidity at saturation (kg kg^{-1}) at the surface skin temperature $T_{sk,i}$ (in K),
- c_p is the heat capacity at constant pressure (J K^{-1} kg^{-1}),
- g is the gravitational acceleration (= 9.8 m s^{-2}),
- z_a is the air temperature measurement height (= 2 m),
- r_{ai} the aerodynamic resistance of the i^{th} tile (s m^{-1}).
- r_{ci} the canopy resistance of the i^{th} tile (s m^{-1}).

Aerodynamic resistance The aerodynamic resistance is directly connected to the stability of the atmosphere (Eq. 24). Therefore, knowledge of the friction velocity (u_{*i}; m s^{-1}) and the Obukhov length (L_i, m) values are needed and expressed in Eq. 25 and Eq. 26, respectively. The inverse of the aerodynamic resistance is defined as following:

$$\frac{1}{r_{a_i}} = \frac{k u_{*i}}{\ln\left(\frac{z_a - d}{z_{0hi}}\right) - \psi_h\left(\frac{z_a - d}{L_i}\right) + \psi_h\left(\frac{z_{\mathrm{Ohi}}}{L_i}\right)} \tag{24}$$

with,

$$u_{*i} = max\left\{ 0.2, \frac{k U_a}{\ln\left(\frac{z_t - d_i}{z_{0mi}}\right) - \psi_m\left(\frac{z_t - d_i}{L_i}\right) + \psi_m\left(\frac{z_{\mathrm{Omi}}}{L_i}\right)} \right\} \tag{25}$$

and

$$L_i = \frac{\rho_a u_{*i}^3}{\mathrm{kg}\left(\frac{H_i}{c_p T_a} + 0.608 \frac{LE_i}{L_v}\right)} \tag{26}$$

where, d is the displacement height, k the von Kármán constant (= 0.4), Ua the wind speed at 10 meter (m s^{-1}). ψ_h and ψ_m are, respectively, the sensible heat and momentum stability functions, as described in Beljaars and Viterbo (1994) [96]; z_{om} and z_{oh} are, respectively, the roughness length for momentum (in meter) and the roughness length for heat (in meter). Finally, z_t is the air temperature measurement height (= 2 m) and z_a is the the wind speed measurement height (= 10 m). In practice we consider here a flat surface, having the roughness of the different surface types, without further consideration of the displacement height (= 0 m).

Sensible and latent heat fluxes are needed in Eq. 26 to compute the Obukhov length, thus the complete system of non-linear equations has to be solved iteratively.

The roughness length for momentum is calculated as following [97]:

$$z_{\mathrm{om}} = max(0.01,\ 0.013 \times Hl) \tag{27}$$

with, Hl (unit m) the height would depend on the vegetation type and LAI as follows.

For bare soil, snow, rocks and inland water cases:

$$Hl = 0.001 \tag{28}$$

for crop case:

$$Hl = min\left(1.0,\ exp\left(\frac{\mathrm{LAI}_i - 3.5}{1.3}\right)\right) \tag{29}$$

for irrigated crop case:

$$Hl = min\left(2.5,\ exp\left(\frac{\mathrm{LAI}_i - 3.5}{1.3}\right)\right) \tag{30}$$

for grass, bogs and marshes cases:

$$Hl = max\left(0.01,\ exp\left(\frac{\mathrm{LAI}_i}{6}\right)\right) \tag{31}$$

for city case:

$$Hl = 1 \tag{32}$$

for deciduous broadleaved trees, evergreen broadleaved trees and evergreen needleleaved trees cases:

$$Hl = max\left(10,\ min(h_{\mathrm{tree}}, 30)\right) \tag{33}$$

with, h_{tree} the height in meter of the trees. Finally, the roughness length for heat z_{oh} is obtained by dividing z_{om} by 100 for bare soil, deciduous broadleaved trees, evergreen needleleaved trees, rocks and city surface types and by 10 for other ones [83, 97].

Canopy resistance to transpiration The formulation of the canopy resistance r_c (s m^{-1}) of the vegetation to transpiration is based on van den Hurk et al. (2000). Change has been made in the parametrisation for crops and non-perennial grasslands to introduce more sensitivity of the model for low green biomass conditions. Thus, the canopy resistance formulation will depend on the surface type. For evergreen needleleaved trees and evergreen broadleaved trees, deciduous broadleaved trees, crops, irrigated crops, grass cases:

$$r_c = \frac{r_{s,min}}{\mathrm{LAI}_i} f_1(SIS) f_2() f_3(D_a) \tag{34}$$

$\mathrm{r_c}$ is set to 1000 for snow and city cases and to 0 for bog/marches and inland water cases. Specific parametrisation for bare soil and rock cases will be presented below.

In the Eq. 34, the Jarvis functions, $f_{1,2,3}$ parameterize the dependency of the transpiration limitation to basic environmental variables. Thus, the minimum stomatal resistance scaled by LAI_i set the maximum rate of evapotranspiration observed for each vegetation. f_1 expresses the limitation due to the illumination of the active canopy (Eq. 35), f_2 the limitation caused by a shortage of water in the soils (Eq. 36-38) and f_3 the limitation for trees due to water vapour deficit in the atmosphere (Eq. 39):

$$f_1(SIS)^{-1} = min\left(1, \frac{b \times SIS + c}{a \times (b \times SIS + 1)}\right) \quad (35)$$

with, a = 0.81, b = 0.004 and c = 0.05 [47]. Concerning f_2, f_3 and f_4 : If $\geq \theta_{\text{fc}}$

$$f_2(\theta_i)^{-1} = 1 \quad (36)$$

if $\theta_{\text{pwp}} << \theta_{\text{fc}}$

$$f_2(\theta_i)^{-1} = \frac{-\theta_{\text{pwp}}}{\theta_{\text{fc}} - \theta_{\text{pwp}}} \quad (37)$$

and if $\leq \theta_{\text{pwp}}$

$$f_2(\theta_i)^{-1} = 10^{-10} \quad (38)$$

$$f_3(D_a)^{-1} = exp(-g_D \times D_a) \quad (39)$$

where, g_D and D_a are, respectively, a sensitivity coefficient for the dependence of the canopy resistance on water vapor pressure deficit (equal to 3.10^{-4} Pa^{-1} for Deciduous Broadleaved trees, Evergreen Needleleaved trees and Evergreen Broadleaved trees cases and 0 for others) and the atmospheric water pressure deficit D_a which is defined as following:

$$D_a = e_w(T_a) \times (1.0 - Rh) \quad (40)$$

Soil surface resistance For bare soil and rock tiles, the resistance of the canopy r_c needed to estimate the latent energy with Eq. 22 is replaced by r_{soil} obtained from Eq. 41. A minimum stomatal resistance (rs_{min}; Table 5) is associated to bare soil and rock to represent the minimum soil resistance and the only stress for evaporation is due to soil water deficit, via a modified Jarvis function $f_{2,BS}$which allows a broader range of soil moisture sensitivity:

$$r_{\text{soil}} = r_{s,min} \times f_{2,BS}\left(f_{liq,1} \times \theta_1\right) \quad (41)$$

with,

$$f_{2,BS}\left(f_{liq,1}, \theta_1\right) = 1 + \left(\frac{1000 \times \left(f_c - f_{\text{pwp}}\right) + 1}{\exp\left(50 \times \left(f_{\text{liq}} \times \theta_1 - \theta_{\text{pwp}}\right)\right)}\right) \quad (42)$$

C. Calculation at the pixel level

C.1. Instantaneous products

Surface heat flux values for the whole pixel are calculated as a weighted contribution of the different tiles:

$$\text{LE} = \sum \xi_i \text{LE}_i \quad (43)$$

and

$$H = \sum \xi_i H_i \quad (44)$$

and

$$G = \sum \xi_i G_i \quad (45)$$

with xi_i is the fraction of i tile in the pixel. *LE and H* are calculated for the whole pixel and are expressed in W m^{-2}.

From the latent energy, the evapotranspiration ET rate, expressed in $mm.h^{-1}$, is given by:

$$\text{ET} = \frac{3600 \times \text{LE}}{L_v} \quad (46)$$

with L_v the latent heat of vaporization in J Kg^{-1} is:

$$L_v = [2.501 - 0.00234 \times (T_a - 273.15)] \times 10^6 \quad (47)$$

For snow, the latent heat of sublimation is used which includes the additional phase transformation from solid to liquid (fusion):

$$L_s = L_f + L_v \quad (48)$$

where, L_f = 0.334 $.10^6$ J kg^{-1}.

D. Iterative solver

For each tile, solving the system of equations requires an iterative method, because of the strong non-linear inter-dependence of the variables H, LE, T_{sk} and u_*. In the implementation, a single point iteration method has been selected for solving the system of equations, assuming neutral stability as a condition. Iterations start with an initialisation of H, LE, T_{sk}, u_*values and is stopped when the estimates of the three key-variables (H, LE, T_{sk}) are stabilized, using a predefined precision criterion (difference between two successive iterations less than 0.1 W m^{-2} for H and LE and 0.01 K for T_{sk}). Initial values are set to H = 0 W m^{-2}, LE = 0 W m^{-2}, T_{sk} = 273.15 K and u_* = 0.5 m s^{-1}. Thereafter, the starting point is set from the previous iterated pixel are used. When the number of iterations exceeds 100, the process is stopped and algorithm returns the flag 'not-converged'.

ADD or not?

E. Spatio-temporal averaging

E.1. Temporal integration

The hourly integration is done with piecewise linear integration between the measurements done during the 1 hour interval, considering also the measurement done just before and just after the interval.The missing data are temporally interpolated over up to 3-hour.

For each pixel, the daily mean is computed from the 24 hourly integrations. In case one or several of these 24 values are missing (it was not possible to fill a gap by interpolation), the daily mean pixel is set to the fill-value. If this occurs for all the pixels, the day is flagged as 'incomplete' and no daily mean product will be issued (this flag is also used to discard the day in the monthly averaging, see after).

From the hourly data, the diurnal cycle is computed as the average of the available hourly values for the calendar month. To avoid introduction of discontinuity in the diurnal cycle, only the days which are not flagged as incomplete are considered. A minimum number of 15 days is required to compute each hourly interval of the diurnal cycle (at the pixel level). If the 15 days criterion of available hourly integrations is not met for all the pixels, the diurnal cycle is flagged as 'incomplete' and no monthly mean will be issued for this hourly interval.

Finally, the monthly mean is evaluated as simple averaging of the diurnal cycle. In case one or several of the 24 monthly 1-hourly means are missing (it was set to incomplete), the monthly mean pixel is set to the fill-value. If this occurs for all the pixels, the month is flagged as 'incomplete' and no monthly mean product is issued.

E.2. Spatial re-gridding

To ensure consistency with other CM SAF products, ET, LE and H products are re-gridded on a common regular latitude-longitude grid at a spatial resolution of 0.05°. To perform the transformation, a twin target image is built in which each target pixel has a list of the corresponding pixels in the source image and their associated weights. The re-gridding is performed supposing the energy (density of flux) equally distributed in the original pixel. This assumption allows estimating the re-gridded pixel flux using the surface intersection as weighting of the original pixel flux densities.

After re-gridding, the spatial coverage may be limited, e.g. to 60°N - 60°S and 60°W- 60°E. This will be decided in view of the validation results.

B. FLUXNET SITES

Table 7 provides information about the 30 selected stations for validations.

Author contributions. All authors have been involved in the project, either to provide inputs, review the algorithm or interpretation of the results.

Acknowledgements. This work has been funded by ...

Table 7. Information about *in situ* selected stations used to validate the CM SAF product.

Name	SITE_ID	longitude	latitude	Country	Elevation (m)	IGBP	Area	Climate
Ankasa	GH-Ank	-2.69421	5.26854	GH	124.0	EBF	NAfr	Am
Brasschaat	BE-Bra	4.51984	51.30761	BE	16.0	MF	Euro	Cfb
Demokeya	SD-Dem	30.4783	13.2829	SD	500.0	SAV	NAfr	BWh
Fontainebleau Barbeau	FR-Fon	2.7801	48.47636	FR	103.0	DBF	Euro	Cfb
Fyodorovskoye	RU-Fyo	32.92208	56.46153	RU	265.0	ENF	Euro	Dfb
Hainich	DE-Hai	10.45217	51.07921	DE	430.0	DBF	Euro	Cfb
Hyytiala	FI-Hyy	24.29477	61.84741	FI	181.0	ENF	Euro	Dfc
Klingenberg	DE-Kli	13.52238	50.89306	DE	478.0	CRO	Euro	Cfb
Le_Bray	FR-LBr	-0.7693	44.71711	FR	61.0	ENF	Euro	Cfb
Lettosuo	FI-Let	23.95952	60.64183	FI	111.0	ENF	Euro	Dfb
Lonzee	BE-Lon	4.74623	50.55162	BE	167.0	CRO	Euro	Cfb
Loobos	NL-Loo	5.74356	52.16658	NL	25.0	ENF	Euro	Cfb
Monte Bondone	IT-MBo	11.04583	46.01468	IT	1550.0	GRA	Euro	Dfb
Oberbärenburg	DE-Obe	13.72129	50.78666	DE	734.0	ENF	Euro	Cfb
Puechabon	FR-Pue	3.5957	43.7413	FR	270.0	EBF	Euro	Csa
Selhausen	DE-Seh	6.44965	50.87062	DE	103.0	CRO	Euro	Cfb
Selhausen Juelich	DE-RuS	6.44714	50.86591	DE	102.755	CRO	Euro	Cfb
Skukuza	ZA-Kru	31.4969	-25.0197	ZA	359.0	SAV	SAfr	Cwa
Sodankyla	FI-Sod	26.63859	67.36239	FI	180.0	ENF	Euro	Dfc
Tharandt	DE-Tha	13.56515	50.96256	DE	385.0	ENF	Euro	Cfb
Vielsalm	BE-Vie	5.99812	50.30493	BE	493.0	MF	Euro	Cfb
Gebesee	DE-Geb	10.91463	51.09973	DE	161.5	CRO	Euro	Cfb
Neustift	AT-Neu	11.3175	47.11667	AT	970.0	GRA	Euro	Dfc
Grillenburg	DE-Gri	13.51259	50.95004	DE	385.0	GRA	Euro	Cfb
Soroe	DK-Sor	11.64464	55.48587	DK	40.0	DBF	Euro	Cfb
Grignon	FR-Gri	1.95191	48.84422	FR	125.0	CRO	Euro	Cfb
Collelongo	IT-Col	13.58814	41.84936	IT	1560.0	DBF	Euro	Cfa
Lavarone	IT-Lav	11.28132	45.9562	IT	1353.0	ENF	Euro	Cfb
Renon	IT-Ren	11.43369	46.58686	IT	1730.0	ENF	Euro	Dfc
Davos	CH-Dav	9.843558	46.81297	CH	1639.0	ENF	Euro	ET